

¹ Explicit and Mean-Field Models for Coverage-Dependent CO
² Adsorption on Pd(111)

³ John P. Clay,^a Chang Yan,^a Hanyu Ma,^a Steven J. McDonough,^a Kurt Frey,^a Jeffrey P. Greeley,^b
Fabio H. Ribeiro,^b W. Nicholas Delgass,^b and William F. Schneider^{a,c*}

⁴ ^a Department of Chemical and Biomolecular Engineering. 182 Fitzpatrick Hall. University of
⁵ Notre Dame. Notre Dame, IN 46556. USA

⁶ ^b School of Chemical Engineering. 480 Stadium Mall Drive. Purdue University. West Lafayette,
⁷ IN 47907. USA

⁸ ^c Department of Chemistry and Biochemistry. 251 Nieuwland Science Hall. University of Notre
⁹ Dame. Notre Dame, IN 46556. USA

¹⁰

¹¹ **Abstract**

¹² The water gas shift reaction is widely used in industry to convert CO and H₂O to H₂.
¹³ In order to properly model the activity of WGS catalysts, a coverage dependent binding
¹⁴ energy of CO is needed in addition to values for reaction energies, activation energies and
¹⁵ prefactors. In this study, a coverage dependent binding energy of CO is presented. Due
¹⁶ to the complex nature of CO binding, three different cluster expansions were fitted to a
¹⁷ series of DFT calculations of CO on the Pd(111) surface spanning a range of coverages.
¹⁸ A cluster expansion is an Ising type model that fits energies to polynomials of occupation
¹⁹ variables. Once the cluster expansion was fitted, Grand Canonical Monte Carlo simulations
²⁰ were performed to determine the coverage dependent binding energy, and then fitted to
²¹ several different functional forms of coverage. Finally, a mean field model for the temperature
²² programmed desorption spectrum is presented for comparison to experiments.

*Corresponding author: wschneider@nd.edu, +1-574-631-8754

²³ **Keywords**

²⁴ CO; Pd(111); DFT; Cluster Expansions; Monte Carlo Simulation

²⁵ **Highlights**

- ²⁶ • Developed FCC; FCC, and HCP Hollow; and FCC, and HCP Hollow, and Atop cluster
²⁷ expansions for Pd(111)-CO system
- ²⁸ • Three-site CE reproduces observed ordered configurations
- ²⁹ • Coverage-dependent binding energies (saturation coverages, ground states, shapes of bind-
³⁰ ing energy vs coverage) differ significantly in three models
- ³¹ • Propose GCMC strategy to extract coverage-dependent binding energy $E(\theta)$
- ³² • $E(\theta)$ predicts observed CO TPD

³³ **1 Introduction**

³⁴ Under conditions relevant to heterogeneous catalysis the coverage of adsorbates on a catalytic
³⁵ metal surface can be a large fraction of the total number of available sites. Capturing the
³⁶ influence of this coverage is important in developing reliable models of surface adsorption and
³⁷ reaction [1–8]. In a mean-field microkinetic approach, adsorbate coverage-dependent adsorption
³⁸ is described by writing a differential adsorption energy, $\bar{E}_{\text{ads}}(\theta)$, as an explicit function of the
³⁹ surface density of adsorbates, often expressed as a fractional coverage, θ [2–5, 9]. This function
⁴⁰ can be fit to experimental desorption or rate data [10–12], can be inferred through physics-based
⁴¹ empirical models[13, 14] or correlations [15], or can be extracted from a density functional theory
⁴² (DFT) calculations of adsorption energy at a select set of coverages [2, 3]. A common problem
⁴³ that arises in computing $\bar{E}_{\text{ads}}(\theta)$ from DFT is the selection of arrangements, or configurations,
⁴⁴ of adsorbates to use as representative of a particular coverage.

⁴⁵ Recently, cluster expansion (CE) fitting has been integrated with DFT calculations both as
⁴⁶ an aid to identifying low energy adsorbate configurations and as an efficient model of coverage-
⁴⁷ dependent energies[1, 16–19]. The energy of an arrangement, or configuration, σ of adsorbates
⁴⁸ within a CE model is written as a polynomial expansion in occupation variables, σ_i , which in

49 the Ising convention are either 1 or -1 in the presence or absence of an adsorbate at site i ,
 50 respectively:

$$E_{\sigma}^{\text{CE}} = J_0 + \sum_i^{\text{sites}} J_i \sigma_i + \sum_{i>j}^{\text{pairs}} J_{ij} \sigma_i \sigma_j + \sum_{i>j>k}^{\text{3-body}} J_{ijl} \sigma_i \sigma_j \sigma_k + \dots \quad (1)$$

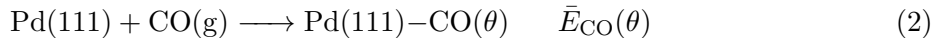
51 The individual terms are conventionally called clusters, and “fitting” of the cluster expansion
 52 involves iteratively building up a database of DFT configuration energies, selecting clusters,
 53 and determining the effective cluster interactions J until some internal consistency criteria are
 54 satisfied [20–22]. This process of iterative CE construction can lead to the discovery of non-
 55 intuitive but important adsorbate arrangements. Further, once converged, the CE allows for
 56 rapid prediction of energies on length scales much larger than accessible directly with DFT. The
 57 first such applications of this approach were to adsorbates on single sites on a hexagonal lattice,
 58 including O/Ru(0001) [1, 23], O/Pt(111) [15, 16, 18, 19], O/Ni(111) [24], O/Au(111) [18], and
 59 O/Pt_{1-x}/Ru_x(111) [17]. CEs have been reported for applied to study adsorbate ordering for
 60 many systems including: CO/Pd(111) [25], O/Pt(321) [20], H/Pt(111) [26], CO/Pt(111) [25,
 61 27], H/Ir(100) [21, 28], H/graphene [29], O/W(110) [30], O/Pd(100) [31], and (CO+O)/Pd(100)
 62 [31], and CO/Pd(100) [31, 32]. However, most of these studies have only focused on adsorp-
 63 tion on a single site, and there is little work where multiple sites compete for adsorbates.
 64 Some these systems include O/Pt(321) [20], H/Pt(111) [26], H/Ir(100) [21, 28], O/W(110) [30],
 65 (CO+O)/Pd(100) [31], and CO/Pd(111) [26]. These multiple site CEs vary from a two-site CE
 66 for H/Pt(111) to a five-site CE for O/Pt(321). For Pt(321), a five-site CE, oxygen is allowed
 67 to adsorbed in in one of five possible sites on the (1×1) supercell of the (321) surface [20].

68 Water gas shift ($\text{CO} + \text{H}_2\text{O} \rightleftharpoons \text{CO}_2 + \text{H}_2$) catalysis on Pd and Pt is one example of chemistry
 69 in which surface coverage plays a prominent role. CO binds strongly to Pd and Pt surfaces.
 70 Several groups have used infrared spectroscopy to show that CO is near the saturation coverage
 71 under typical WGS conditions on both Pt and Pd [33–40]. Grabow *et al.* found it necessary to
 72 incorporate a coverage-dependent CO binding energy into a DFT-based microkinetic model for
 73 WGS over Pt [2]. Stamatakis developed a lattice-based kinetic model for WGS over Pt that
 74 incorporated CO coverage dependence into the kinetic parameters and found that inclusion of
 75 the kinetic parameters is required to model the kinetics and the Pt surface is CO covered [41,
 76 42]. We recently reported DFT-parametrized kinetic models for WGS over both Pd(111) and
 77 Pt(111) that revealed both high CO coverages under reaction conditions and the necessity of

78 including a coverage-dependent CO binding energy to realize surface coverages and rates even
79 qualitatively consistent with experiment [43].

80 Both experiment and computation have been used to investigate coverage-dependent CO
81 binding on Pd [10, 25, 43–59]. At 1/3 ML, electron diffraction, infrared spectroscopy exper-
82 iments and DFT calculations have shown CO is in a $(\sqrt{3} \times \sqrt{3})R30^\circ - 1$ CO configuration
83 with CO adsorbed in 3-fold hollow sites [45, 48, 54, 59]. As the CO coverage increases to 1/2
84 ML, early studies involving electron diffraction and infrared spectroscopy suggested that CO
85 is adsorbed in bridge sites [45, 49]. Newer experiments involving photoelectron diffraction and
86 XPS, and DFT calculations have suggested that CO is adsorbed in both FCC and HCP Hollow
87 sites in a $c(4 \times 2) - 2$ CO configuration [46, 47, 50, 54]. As the coverage increases to 3/4
88 ML, saturation coverage determined by temperature programmed desorption (TPD), infrared
89 spectroscopy, electron diffraction and DFT calculations show that CO is adsorbed in a FCC,
90 HCP Hollow and Atop site in a $(2 \times 2) - 3$ CO configuration [10, 44, 49, 54]. Guo and Yates
91 used TPD to examine the CO/Pd(111) system, and found that there are three peaks at 500,
92 300, and 200 K which correspond to ground states at 1/3, 1/2, and 3/5 ML, and the saturation
93 coverage is 3/4 ML [10].

94 In this study, we report DFT results and cluster expansion fits to model coverage-dependent
95 CO adsorption on Pd(111):



96 We contrast models that include single (FCC only), dual (FCC and HCP), and three (FCC,
97 HCP, and atop) candidate adsorption sites. We find that while three-fold sites are populated
98 at low coverage, at increasing coverage all site types are occupied. The net effect is a “buffer-
99 ing” of adsorption energies, so that $\bar{E}_{\text{CO}}(\theta)$ maintains a more constant value over a larger
100 window of coverage than would be inferred from a single-site model. We combine the CE with
101 Grand Canonical Monte Carlo (GCMC) simulations to extract the CO coverage vs. external
102 CO chemical potential at various temperatures. By subtracting off the appropriate mean-field
103 configurational entropy, we extract coverage-dependent binding energies, $\bar{E}_{\text{CO}}(\theta)$, appropriate
104 for mean-field microkinetic models. We illustrate the utility of this function through prediction
105 of the CO desorption TPD spectrum from Pd.

106 **2 Computational Details**

107 **2.1 Density Functional Theory (DFT) Model**

108 The Vienna *ab initio* Simulation Package (VASP) was used to perform plane wave supercell den-
109 sity functional theory (DFT) calculations within the PW91 implementation of the generalized
110 gradient approximation (PW91-GGA) [60–63]. A projector augmented wave (PAW) treatment
111 of core states was used [64, 65]. Plane waves were included up to a kinetic energy cutoff of
112 400 eV. Energies were converged to 10^{-8} eV and forces to 0.03 eV/Å. The bulk Pd lattice con-
113 stant within these approximations is 3.954 Å, which compares well with the experimental value
114 of 3.859 Å [66]. The (111) surface was described with three-layer-thick Pd slabs separated by
115 20 Å of vacuum; the top Pd layer was allowed to relax in all optimizations. The first Brillouin
116 zone was sampled using a KPOINT mesh equivalent to a Γ -centered $8 \times 8 \times 1$ Monkhorst-Pack
117 grid for a 2×2 supercell [67]. We calculated a CO molecule in a $20 \times 20 \times 20$ Å box to have
118 a bond length of 1.141 Å and harmonic frequency of 2131 cm⁻¹, which compare well with the
119 experimental values of 1.12 Å and 2145 cm⁻¹ [68].

120 **2.2 Cluster Expansion (CE) Fitting**

121 We use the cluster expansion (CE) both to identify the most important (low energy) arrange-
122 ments of CO and to model the coverage-dependent adsorption energies.

123 The relationship between the FCC, HCP, and atop triangular sublattices is shown in Figure
124 1. For each combination of sublattices, we first identified a large set of candidate adsorbate
125 arrangements by enumerating all possible unique configurations, starting with the primitive
126 unit cell (1×1) and increasing the supercell size until a maximum sized supercell of (5×5)
127 (25 FCC Hollow site, 25 HCP Hollow sites, 25 Atop sites), using the *genstr* script within the
128 Alloy Theoretic Automated Toolkit (ATAT) [69–72]. We then selected a small number of these
129 structures as seeds for the fitting process. For each seed configuration, σ , we compute the total
130 DFT energy, $E_{\sigma}^{\text{DFT}}(\phi)$, and the formation energy, ΔE_F , relative to the clean surface according
131 to

$$\Delta E_F(\sigma) = \frac{1}{N_M(\phi)} \left[E_{\sigma}^{\text{DFT}}(\phi) - E_{\text{clean}}^{\text{DFT}}(\phi) - N_A(\sigma) E_{\text{CO(g)}}^{\text{DFT}} \right] \quad (3)$$

132 where $E_{\text{clean}}^{\text{DFT}}(\phi)$ is the DFT energy of an adsorbate-free surface calculated in the identical

¹³³ supercell, $N_M(\phi)$ is the number of surface Pd atoms in the supercell, $E_{A(g)}^{\text{DFT}}$ is the DFT energy
¹³⁴ of the gas phase DFT CO molecule, and $N_A(\sigma)$ is the number of adsorbed CO molecules [22].

¹³⁵ The CE expands these formation energies in the spin variable products, or “clusters,” and
¹³⁶ effective cluster interactions J as shown in Eq. 1. To select clusters for a particular fit, we
¹³⁷ considered a pool of candidate 2-, 3-, and 4-body clusters within the radii in Table 2 and used
¹³⁸ a steepest descent algorithm to identify the the minimum number of clusters that fit the DFT
¹³⁹ formation energies [73]. We used a cross-validation (CV) score (S_{CV}) to evaluate the predictive
¹⁴⁰ quality of the fit, where n is the number of points, E_i is calculated energy and $E_{(i)}$ is the fitted
¹⁴¹ energy [72, 74–76].

$$S_{\text{CV}} = \left(\frac{1}{n} \sum_i^n (E_i - E_{(i)}) \right)^{\frac{1}{2}} \quad (4)$$

¹⁴² Fitting was considered converged when the CV score fell below 10 meV Å⁻². The fitted CE
¹⁴³ was then used to predict the formation energies of all the structures in the structure database.
¹⁴⁴ If any of the predicted energies had formation energies below the DFT formation energy hull,
¹⁴⁵ the DFT formation energy was added to the DFT database, and the CE was refitted. This
¹⁴⁶ procedure was repeated until none of the predicted energies fell below the DFT formation
¹⁴⁷ energy hull.

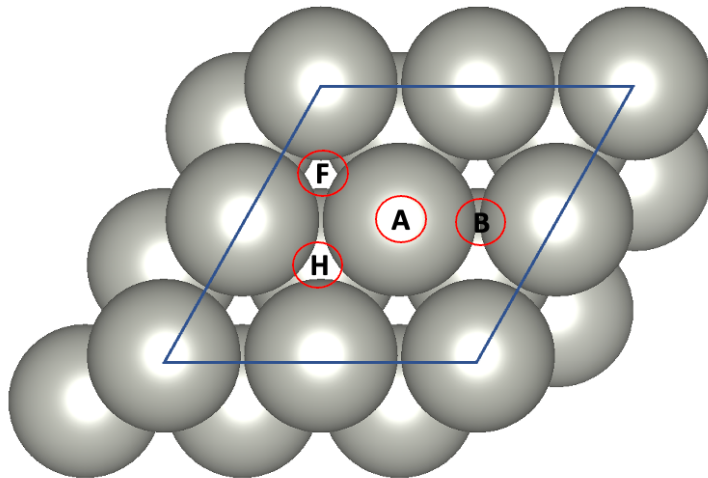


Figure 1: Geometric relationship between FCC, HCP, and Atop sites in the (2 × 2) supercell (blue lines) on the (111) surface of a close-packed metal. (F), (H), (A) and (B) represent FCC, HCP, Atop, and Bridge sites respectively.

Table 1 Binding energies, C–O bond lengths, and vibrational frequencies of CO at 1/3 ML in a $(\sqrt{3} \times \sqrt{3})R30^\circ - 1$ CO Configuration

Binding Site	Binding Energy	C–O Bond Length (Å)	Vibrational Frequency (cm ⁻¹)
FCC Hollow	−2.00	1.185	1820
HCP Hollow	−2.01	1.185	1822
Bridge	−1.81	1.177	1878
Atop	−1.47	1.156	2063

148 2.3 Grand Canonical Monte Carlo (GCMC) Simulations

149 GCMC simulations were performed on the converged CE Hamiltonians with the Easy Monte
 150 Carlo Code (emc2) within ATAT [70]. The GCMC simulations provide information about
 151 coverage as a function of chemical potential (μ_{CO}), surface area A and temperature T . We
 152 performed GCMC simulations in a 42×42 supercell (1764 FCC Hollow sites, 1764 HCP Hollow
 153 sites, and 1764 Atop sites) from 100 K to 900 K and over a range of chemical potentials
 154 spanning coverages from 0 to ≈ 1 CO/surface Pd. The calculations were initialized in a random
 155 configuration and the GCMC moves involve “flipping” a site between occupied and unoccupied
 156 states and were converged when the average coverage between steps i to j and k to l were within
 157 10^{-5} ML of each other.

158 3 Cluster Expansion Results

159 3.1 Comparison of CO Binding Sites

160 To calibrate calculations, CO binding in FCC, HCP, atop and bridge sites were compared at
 161 1/3 ML in a $(\sqrt{3} \times \sqrt{3})R30^\circ - 1$ CO configuration (Table 1). CO has similar binding energies,
 162 vibrational frequencies and C–O bond distances in the FCC and HCP sites, the bridge site
 163 is slightly less stable, and the atop site is the least stable by about 0.5 eV over FCC/HCP.
 164 The generalized gradient approximation tends to exaggerate the preference of CO for high
 165 coordination sties [77, 78]. However electron diffraction, vibrational spectroscopy and previous
 166 DFT calculations confirm the preference of CO for three-fold hollow sites at 1/3 ML [45, 54,
 167 59].

Table 2 Summary Cluster Expansion Parameters

CE Data	FCC	FCC/HCP	FCC/HCP /Atop
Cluster Size (Å)			
Pair	12.5	12.5	12.5
3-Body	12.5	10.0	10.0
4-Body	6.0	10.0	10.0
Structure Database	3164	6708	12280
Cluster Database	131	870	1067
Initial Number of Structures Included	25	63	50
Iterations	3	21	6
Final Number of Structures Included	58	183	193
Clusters Included	3	47	43
CV Score (meV/Å ²)	7.59	9.62	9.08

168 3.2 Construction of Cluster Expansions

169 3.2.1 FCC-only Model

170 We next considered coverage-dependent CO binding using a CE limited to the FCC sites as
 171 candidate coordination sites. Table 2 contains the details of the FCC-only CE fitting procedure.
 172 We selected 25 seed structures from an initial candidate pool of 3164 possible structures and
 173 iterated the CE fitting procedure 3 times to arrive at a final, self-consistent CE. The DFT
 174 database included at the end 58 structures, and the CE contains only one non-trivial two-body
 175 interaction (Table S1).

176 Figure 2 C compares the GGA-computed formation energies with the CE predictions. The
 177 two-body-only CE fits the data with a cross validation score of 7.59 meV/Å². Figure 2 A shows
 178 the DFT-computed formation energies. The minimum energy hull has two “kinks” at 1/3 and
 179 2/3 ML corresponding to a $(\sqrt{3} \times \sqrt{3})R30^\circ - 1$ CO (Figure 3 A) and a $(\sqrt{3} \times \sqrt{3})R30^\circ - 2$
 180 CO configuration (Figure 3 B), respectively. Figure 3 C includes for completeness the $(1 \times$
 181 1) structure. The slope of the formation energy hull is the 0 K differential binding energy,
 182 $\bar{E}_{CO}^{FCC}(\theta, 0 \text{ K})$, and is plotted in Figure 2 B. The 0 K differential binding energy is constant
 183 to 1/3 ML, up to which coverage each adsorbate can avoid any first nearest neighbor (1NN)
 184 interactions, steps up above 1/3 ML as each new adsorbate accumulates three 1NNs, and steps
 185 up again to a positive value above 2/3 ML, where each new adsorbate acquires 6 1NNs. Table 3
 186 summarizes the ground state geometries in this model and Supplementary Section S1 provides
 187 the CE details.

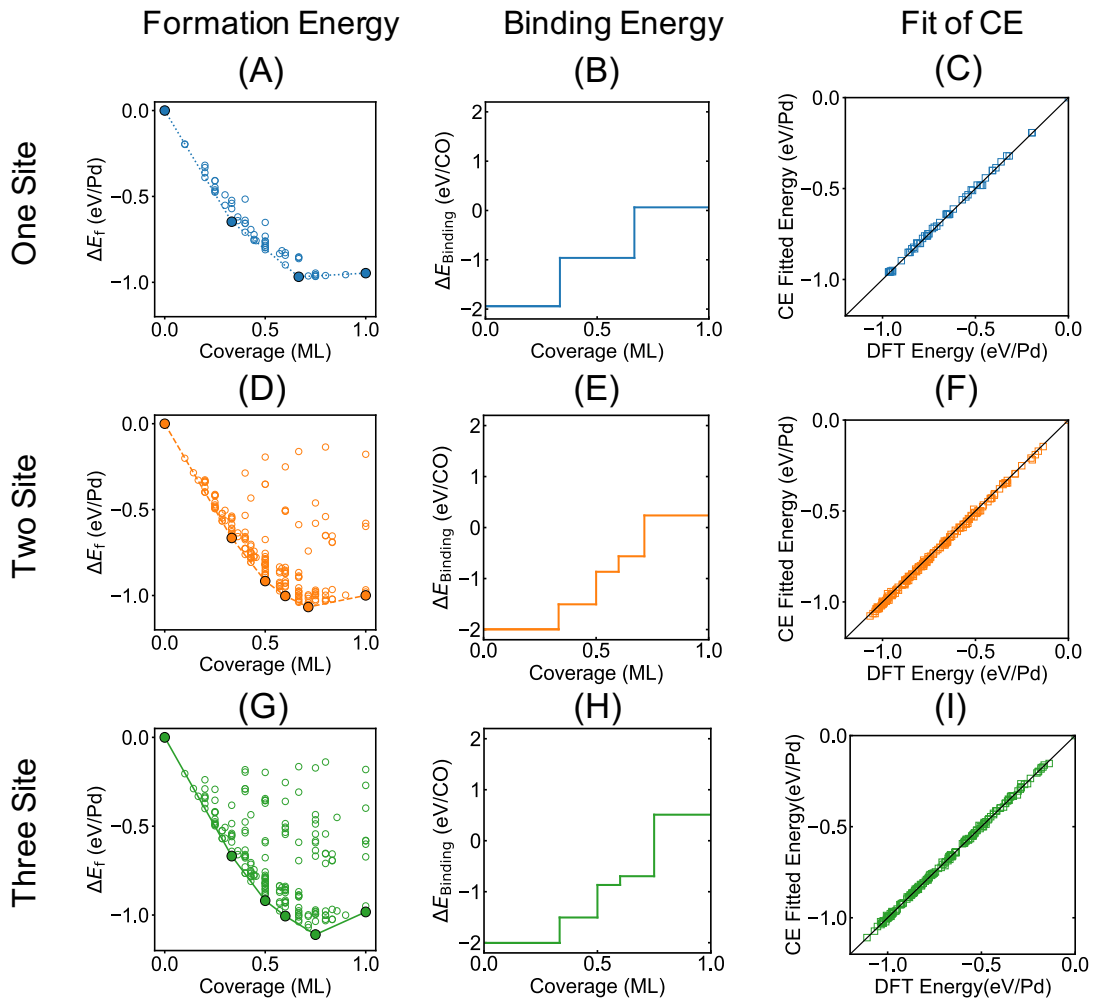


Figure 2: First column: GGA-computed formation energies vs. coverage for FCC-only, FCC/HCP, and FCC/HCP/atop models from top to bottom. Middle column: differential binding energy vs. coverage for same three models. Last column: CE fitted vs. DFT-computed formation energies for same three models.

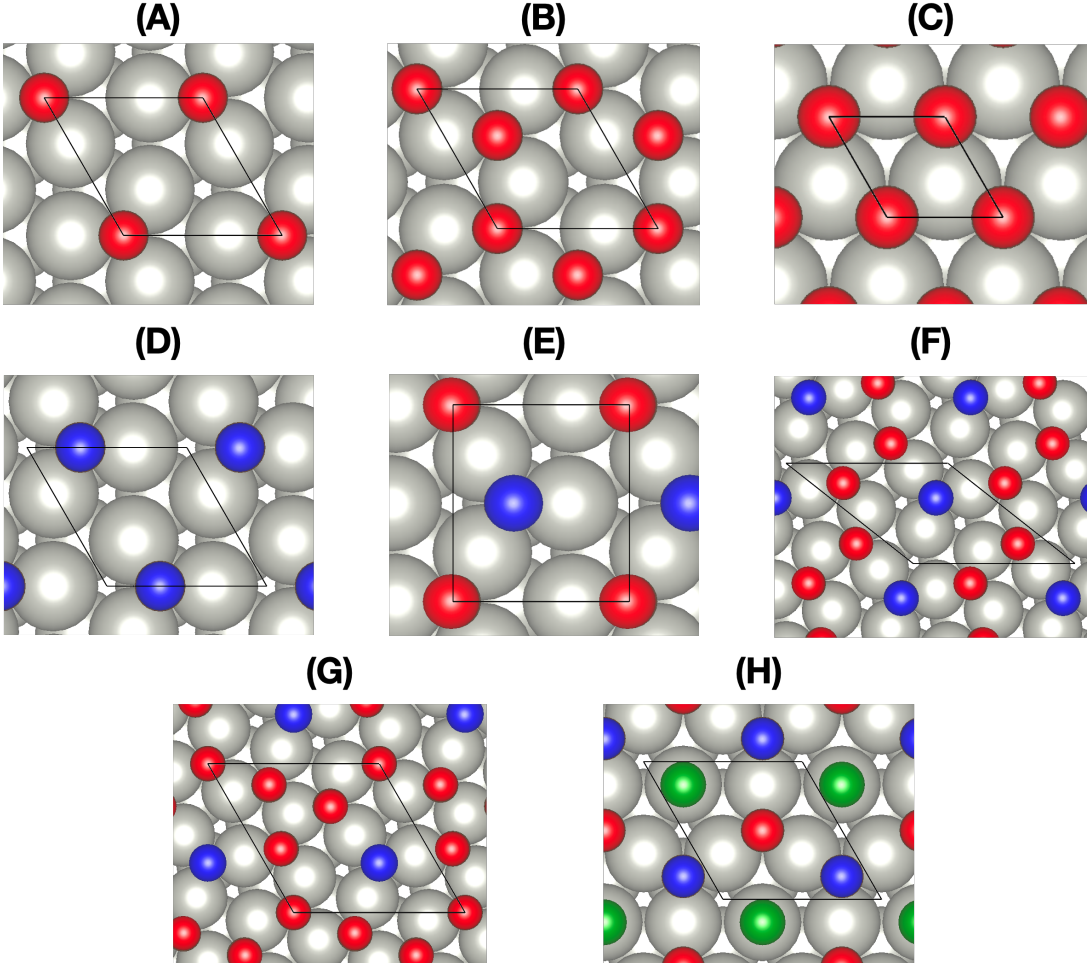


Figure 3: Top view of computed ground state structures. Red, blue and green correspond to FCC, HCP, and atop sites, respectively. (A) 1/3 ML FCC, (B) 2/3 ML FCC, (C) 1 ML FCC, (D) 1/3 ML HCP Hollow, (E) 1/2 ML FCC/HCP, (F) 3/5 ML FCC/HCP, (G) 5/7 ML FCC/HCP, and (H) 3/4 ML FCC/HCP/ATOP. Black lines represent the unit cell.

188 3.2.2 FCC/HCP Model

189 We next considered CO co-adsorption in FCC and HCP sites. In principle, these two sublattices
190 together can accommodate up to two CO molecules per surface Pd atom. Adjacent FCC and
191 HCP sites are separated by only 1.615 Å, and test calculations show that two CO placed this
192 close to one another relax spontaneously to more remote sites. We estimate this 1NN FCC-HCP
193 interaction energy to be approximately 2 eV, greater than the absolute CO binding energy at low
194 coverage. Above a coverage of 1 CO molecule per surface Pd these 1NN FCC-HCP interactions
195 are unavoidable. Further tests show that at these high coverages, CO molecules near the surface
196 relax to unphysical structures in which the C–O bond is broken. Thus, we found it necessary
197 to exclude all FCC/HCP structures with a total coverage > 1 ML and, to obtain energies useful

Table 3 Geometric Data for the FCC Hollow Site Cluster Expansion Ground States.

Coverage (ML)	Geometry
1/3	$(\sqrt{3} \times \sqrt{3})R30^\circ - 1$ CO
2/3	$(\sqrt{3} \times \sqrt{3})R30^\circ - 2$ CO
1	(1 × 1)-1 CO

for inclusion in the DFT database, to laterally constrain CO pairs in 1NN FCC-HCP adjacency in configurations below 1 ML.

Table 2 contains the results of the cluster expansion fitting procedure. We initially selected 63 structures from a candidate pool of 6708, including all the structures from the FCC-only calculations and additional HCP-only and mixed configurations. The fitting procedure took 21 cycles to converge to a self-consistent CE. A total of 183 DFT structures were computed, and the final CE including 47 clusters had a CV score of 9.62 meV Å⁻² (Table S2). Figure 2 F shows that the CE reproduces the DFT numbers uniformly well. The inclusion of FCC and HCP sites together yields a richer formation energy hull, shown in Figure 2 D. The ground state at 1/3 ML remains and has the same $(\sqrt{3} \times \sqrt{3})R30^\circ - 1$ CO structure, although as expected from the comparisons in Table 1, with CO in HCP sites (Figure 3 D). A new ground state appears at 1/2 ML in which half the CO occupy FCC and half HCP sites, each CO sublattice having c(4 × 2) symmetry (Figure 3 E). In this configuration half the surface Pd have two CO in opposing (second nearest neighbor, 2NN) FCC and HCP sites and the other half have either a single FCC or HCP CO. Another new ground state appears at 3/5 ML (Figure 3 F) in which 2/3 of the CO occupy FCC and 1/3 HCP sites. Here the FCC CO form chains of adjacent occupied sites like that in the 2/3 ML FCC-only structure, with the chains separated by intervening rows of HCP CO. The more dense 2/3 ML FCC-only ground state disappears in the FCC/HCP system. In its place appears a 5/7 ML structure (Figure 3 G) in which 4/5 of the CO occupy FCC and 1/5 HCP sites. The structure is more complex, but the 2NN FCC-HCP motif is retained. At 1 ML the FCC-only configuration is lower in energy than HCP-only; any mixed configuration would have high energy 1NN CO. As evident from Figure 2 D, many other configurations are close in energy to the ground state hull. Figure 2 E plots the differential binding energy $\bar{E}_{CO}^{F/H}(\theta)$ extracted from the ground state hull. Energies increase in more gradual steps than in the FCC-only model up to 5/7 ML, where $\bar{E}_{CO}^{F/H}(\theta)$ jumps to a strongly positive value. Table 4 summarizes the structures for the ground states and Supplemental Section S2

Table 4 Geometric Data for the FCC and HCP Hollow Site Cluster Expansion Ground States.

Coverage (ML)	Geometry
1/3	$(\sqrt{3} \times \sqrt{3})R30^\circ - 1$ CO
1/2	c(4 × 2)–2 CO
3/5	$ a = b = 7.399 \text{ \AA}$, $\psi = 141.78^\circ$
5/7	$ a = b = 7.399 \text{ \AA}$, $\psi = 120.00^\circ$
1	(1 × 1)–1 CO

²²⁴ contains details of the FCC/HCP CE.

²²⁵ 3.2.3 FCC/HCP/Atop Model

²²⁶ We next consider CO adsorption into FCC, HCP, and atop sites (Figure 1). In principle, these
²²⁷ three sublattices can accommodate up to three CO per surface Pd atom. First-nearest-neighbor
²²⁸ separations between any pair of sublattices is 1.615 Å. Test calculations report results similar
²²⁹ results to those above; any 1NN pairing is of very high energy, unstable, and unimportant.
²³⁰ Again we prune from the DFT database all structures with > 1 ML coverage and constrain
²³¹ the positions of 1NN pairs to preserve site occupancies at < 1 ML. Table 2 contains the results
²³² of the converged cluster expansion. The candidate pool includes 12280 candidate DFT struc-
²³³ tures, which included all of the strucutres from the previous models, plus atop-only and mixed
²³⁴ (FCC/HCP/atop) configurations. We started with 50 initial structures, chosen at random. The
²³⁵ CE fitting procedure converges after 6 iterations and the computation of a total of 193 DFT
²³⁶ structures.

²³⁷ Fitting only requires ten more DFT energies and four fewer clusters to obtain a cross vali-
²³⁸ dation score of 9.08 meV/Å². Figure 2 I shows a comparison of the DFT computed formation
²³⁹ energies with the cluster expansion predicted formation energies. Figure 2 G shows the DFT
²⁴⁰ formation energies with the formation energy hull, where there are “kinks” at 1/3, 1/2, 3/5, and
²⁴¹ 3/4 ML, which correspond to the ground states. The ground states at 1/3, 1/2, 3/5 and 1 ML
²⁴² are the same ground states determined in by the FCC, and HCP Hollow site cluster expansion
²⁴³ (Figure 3 C-F). A new ground state at 3/4 ML has CO adsorbed in a FCC Hollow, HCP Hollow
²⁴⁴ and Atop site. Figure 2 H shows the 0 K differential binding energy, where there are steps at 0,
²⁴⁵ 1/3, 1/2, 3/5, and 3/4 ML. At 3/4 ML, the 0 K differential binding energy becomes positive,

Table 5 Geometric Data for the FCC, HCP Hollow, and Atop Site Cluster Expansion Ground States.

Coverage (ML)	Geometry
1/3	$(\sqrt{3} \times \sqrt{3})R30^\circ - 1$ CO
1/2	c(4 × 2)–2 CO
3/5	$ a = b = 7.399 \text{ \AA}$, $\psi=141.78^\circ$
3/4	(2 × 2) – 3 CO
1	(1 × 1)–1 CO

246 which is different from the previous models.

247 Table 5 reports the geometric configurations for the ground states, and Section S3 in the
 248 Supplemental Information contains all of the effective cluster interactions, and clusters included
 249 in the converged cluster expansion. Figure S1 in the Supplementary Information shows a com-
 250 parison of the formation energies for the different models, and Figure S2 in the Supplemental
 251 Information shows a comparison of the differential binding energies for the different models

252 3.3 Comparison to Previous Work

253 The full cluster expansion construction procedure successfully recovers the known ground states
 254 of CO on Pd(111). In particular, the three most prominent ground states, as judged by the
 255 magnitude of the discontinuities in the coverage-dependent binding energy (Figure 2 H), includ-
 256 ing the HCP-only configuration at 1/3 ML, the mixed FCC/HCP configuration at 1/2 ML, and
 257 the FCC/HCP/Atop configuration at 3/4 ML, all correspond with configurations observed by
 258 electron diffraction [45, 47, 50] and infrared spectroscopy [48, 49] as well as DFT [46, 54, 58].
 259 The CE predicts a more minor ground state at 3/5 ML that to our knowledge has not been
 260 observed.

261 Chen [25] recently reported a cluster expansion for CO on Pd(111). The CE included FCC,
 262 HCP, Atop, and bridge sites, was fitted against 94 pre-selected configurations computed using
 263 the RPBE functional, and included only two-body interaction terms. The RPBE functional
 264 produces an approximately constant offset of 0.2 eV/CO in binding energy relatively to the
 265 PW91 functional used here.[55] The qualitative features of the predicted hull are similar to those
 266 found here, although the Chen CE contains a larger number of ground states and saturation at

267 a somewhat lower coverage.

268 4 Coverage-Dependent Binding Energies

269 It is common to introduce a coverage-dependent (partial molar) binding energy, $\bar{E}(\theta)$, in mean-
270 field kinetic models. There is however no generally accepted strategy for obtaining the binding
271 energy from first-principles [2–4, 41, 42, 79–82]. A coverage-dependent CO binding energy is
272 necessary to recover WGS kinetics over Pd, Pt and Cu and is often obtained by DFT calculations
273 on a small number of arbitrary adsorbate coverages and configurations [2, 3, 41, 42]. As is
274 evident from the 0 K differential binding energies shown in the middle column of Figure 2 and
275 Supplementary Figure S2, the differential binding energies at the coverages that are relevant to
276 WGS are sensitive to these choices. As is also evident, differentiation of the 0 K energy hull
277 produces discontinuities in coverage-dependent properties that are inappropriate to include in
278 $\bar{E}(\theta)$. Here we extract $\bar{E}(\theta)$ from finite-temperature Monte Carlo simulations.

279 4.1 Determination of $\bar{E}(\theta)$ by GCMC

280 Grand canonical Monte Carlo (GCMC) simulations on the cluster expansion Hamiltonian at
281 temperature T gives the coverage (θ) versus the chemical potential (μ_{CO}). The chemical po-
282 tential is related to the binding energy by:

$$\mu_{\text{CO}}(\theta, T) = \bar{E}_{\text{CO}}(\theta, T) - T\bar{S}_{\text{CO}}(\theta, T) \quad (5)$$

283 where $\bar{E}_{\text{CO}}(\theta, T)$ and $\bar{S}_{\text{CO}}(\theta, T)$ are the partial molar enthalpy and entropy, respectively. Within
284 a single-site mean field model, and considering only configurational entropy, $\bar{S}_{\text{MF}}(\theta, T)$ is given
285 by:[83, 84]

$$\bar{S}_{\text{MF}}(\theta, T) = -k_B T \ln \left(\frac{\theta}{1 - \theta} \right) \quad (6)$$

286 which generalizes to n -sites as

$$\bar{S}_{\text{MF}}(\theta, T) = -k_B T \ln \left(\frac{\theta}{n * (1 - \theta)} \right) \quad (7)$$

287 as derived in Supplementary Section S4. An effective mean-field coverage-dependent binding
288 energy can then be defined as

$$\bar{E}_{\text{CO}}(\theta, T) = \mu_{\text{CO}}(\theta, T) + T\bar{S}_{\text{MF}}(\theta, T) \quad (8)$$

289 4.2 GCMC Results

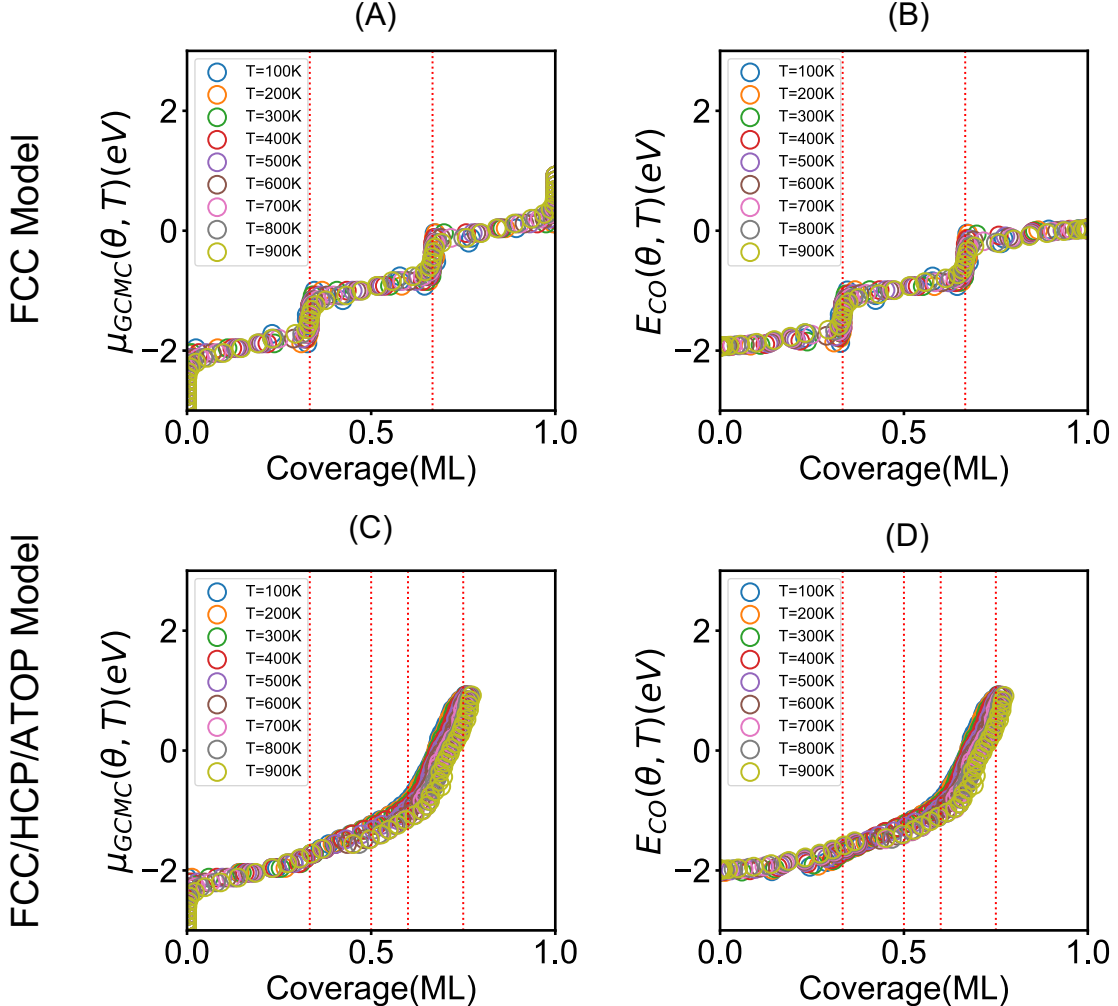


Figure 4: First column: $\mu_{\text{CO}}(\theta, T)$ vs. coverage for FCC model and FCC/HCP/ATOP models from top to bottom at temperature range from 100K to 900K. Last column: $E_{\text{CO}}(\theta, T)$ vs. coverage for the same models.

290 GCMC simulations were performed from 100K to 900K on the one-site and three-site CE models.
 291 Each temperature perform five times and then take average value. Results are shown in Figure
 292 4 A and C, plotted as $\mu_{\text{GCMC}}(\theta, T)$ vs. θ_{CO} . In Figure 4 A, the chemical potential diverges in
 293 the limits of 0 and 1 ML, reflecting the divergence of Eq. 5 in those limits. In Figure 4 C, the
 294 chemical potential diverges in the limits of 0 ML. The one-site model (Figure 4 A) retains the
 295 0 K stair-step pattern smeared out at the boundaries of each ground states. The three site model
 296 (Figure 4 C) shows a qualitatively different gradual rise in chemical potential to approximately

297 0.6 ML, followed by a sharper rise from 0.6 to 0.75 ML. Figure 4 B and D shows $\bar{E}_{\text{CO}}(\theta, T)$ vs.
 298 θ extracted using Eq 8. Subtraction of the mean-field configurational entropy eliminates the
 299 divergences at the extremes of coverage and damps the rise in energy at intermediate coverage.
 300 Further, the sharp discontinuities present in the 0 K differential binding energies are smeared
 301 out at finite temperature. Figure 4 B and D show that the differential binding energies extracted
 302 this way are only weakly temperature dependent.

303 4.3 Coverage-Dependent Binding Energy Models

304 For the purposes of microkinetic modeling it is convenient to represent $\bar{E}(\theta)$ in analytical form.
 305 Piece-wise linear [5], activity [85] and logistic[2] forms have all been applied to obtain analytical
 306 binding energy expression. Here, we fit the one-site and three-site binding energies to the
 307 following analytic functions:

Piece-wise linear: $\bar{E}_{\text{CO}}(\theta) = A$ for $\theta < C$ and $A + B(\theta - C)$ for $\theta \geq C$

$$\text{Activity: } \bar{E}_{\text{CO}}(\theta) = A + B \left\{ \frac{\lambda_1}{1 + \lambda_1 \theta} + \ln \left(\frac{1 + \lambda_2 \theta}{1 + \lambda_1 \theta} \right) + \theta \left[\frac{\lambda_2 - \lambda_1}{(1 + \lambda_2 \theta)(1 + \lambda_1 \theta)} \right] \right\}$$

$$\text{Logistic: } \bar{E}_{\text{CO}}(\theta) = \frac{A}{1 + \exp(B(\theta_{\text{CO}} - C))} + D$$

308 For piecewise function, the data divided to several part by using `scipy.optimize` with Python.
 309 Then implement `polyfit` to obtain piecewise function. For logistic and activity function, `curve_fit`
 310 is employed from `scipy.optimize` package to perform fitting with data. Figure 5 plots the fitted
 311 binding energies against the GCMC-inferred binding energies. Results are summarized in Table
 312 6. Not surprisingly, only Piecewise model is sufficiently flexible to capture the stair-step pattern
 313 of the the FCC-only model (Figure 5 A) with mean absolute error are as small as 0.0397 eV/CO.
 314 But Logistic and Activity model are not able to capture stair-up feature with mean absolute
 315 errors are as large as 0.106 and 0.145 eV/CO. The fits keep fluctuating with coverage increase
 316 and the estimation of binding energy are far from precision.

317 For the three-site model, all of the fits show the same trend in that at low coverages (high
 318 negative bonding energies), the fits correctly estimate the binding energy. At moderate cov-
 319 erages, the fits fluctuate between over and under estimating the binding energies. At high

320 coverages, the all of the fits appropriately estimate the binding energies (Figure 5 D-F). For
 321 the three site model fitting up to a coverage $\theta \approx 0.75$ ML, the largest mean absolute error is
 322 0.126 eV/CO for the Logistic and Activity fit. For determination of the best fit, the Piecewise
 323 functions had the highest R^2 value and the lowest mean absolute error across all the different
 324 models studied for both the one-site and three-site binding energy models.

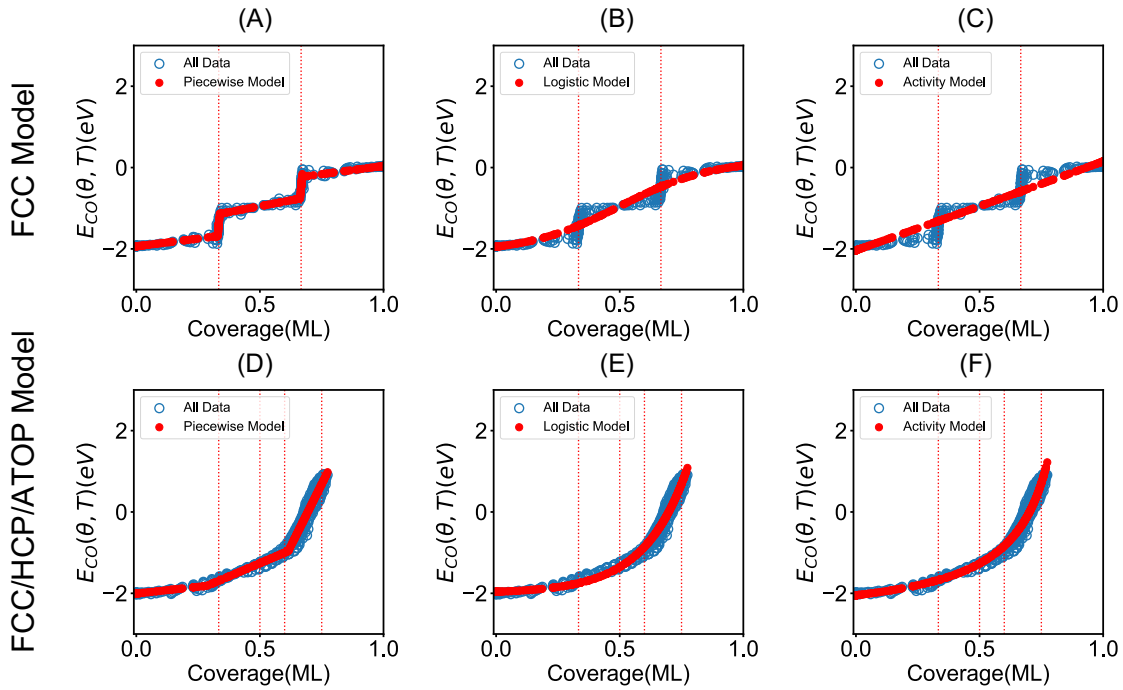


Figure 5: First column: piecewise model fit to all data point. Second column: logistic model fit to all data point. Third column: activity model fit to all data point.

Table 6 Analytical Fitting Result for FCC Model and FCC/HCP/Atop Model

Function	FCC Model			FCC/HCP/Atop Model		
	R^2	MAE	MSE	R^2	MAE	MSE
Piecewise	0.977	0.0397	0.00391	0.975	0.110	0.00224
Logistic	0.958	0.106	0.0218	0.97	0.126	0.0265
Activity	0.938	0.145	0.0323	0.968	0.126	0.0285

325 4.4 Temperature Programmed Desorption (TPD)

326 The CO TPD spectrum on Pd(111) (Figure 6) has been thoroughly studied by Guo and Yates,
 327 and the shape of the TPD reflects the coverage dependent binding energies [10]. In this work
 328 a simulated TPD was generated using the GCMC results for the coverage-dependent binding
 329 energy and all of the analytical fits for coverage dependent binding energy and the first-order
 330 Polyani-Wigner Equation (equation 9), where β is the heating rate (2 K/s), and ν is the prefactor
 331 (10^{13} s $^{-1}$, independent of coverage) [86]. The synthetic TPD can be determined by numerical
 332 integration in steps of 0.2 K starting from 100 K to 800 K and initial coverages varying from
 333 0.1 to 0.6 ML.

$$r_{\text{Des}} = -\frac{\partial \theta}{\partial T} = \frac{\nu \theta}{\beta} \exp\left(-\frac{\bar{E}_{\text{CO}}(\theta)}{k_B T}\right) \quad (9)$$

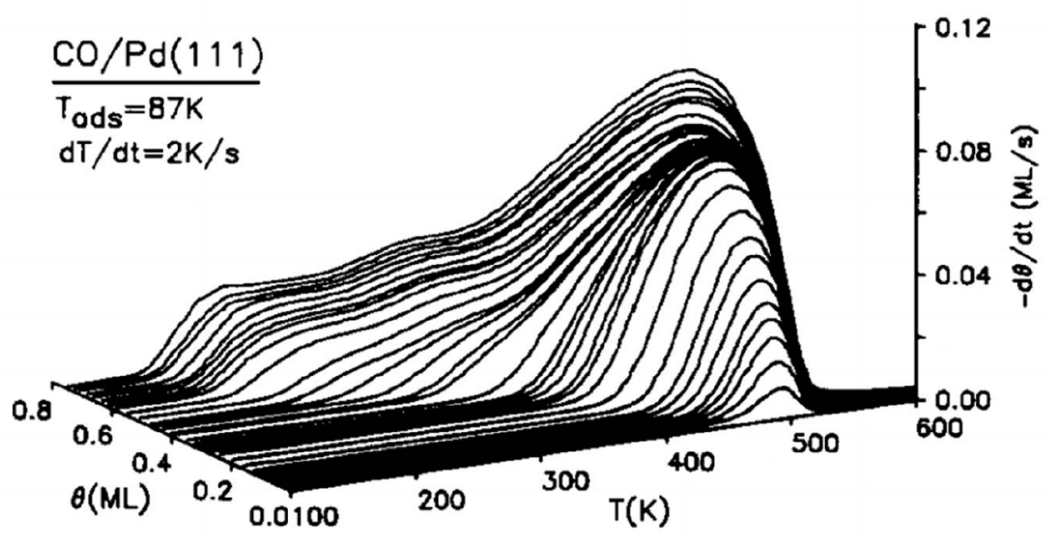


Figure 6: Experimental TPD obtained by Guo and Yates. Heating Rate is 2 K/s, and CO was adsorbed at 87 K. Taken from Reference [10].

334 The simulated TPD spectrum are shown in Figure 7. Figure 7 A-C are TPD spectrum with
 335 different analytical fits of FCC model. As initial coverage up to 0.3 ML, Figure 7 A give a
 336 single peak around 680 K, approximately 180 K higher than the experimental peak which is
 337 due to GGA function tend to overestimate binding strength of CO on Pd [55, 62, 87].As the
 338 initial coverage increases above 0.4 ML, a second sharp peak appears around 350 K. And when
 339 initial coverage keep increasing, the second peak shift to lower temperature. In Figure 7 B,
 340 when initial coverage up to 0.3 ML, single peak occur around 680K but the intensity are same
 341 for 0.2 and 0.3 ML. As initial coverage increase to 0.6 ML, second peak shows up around 250K

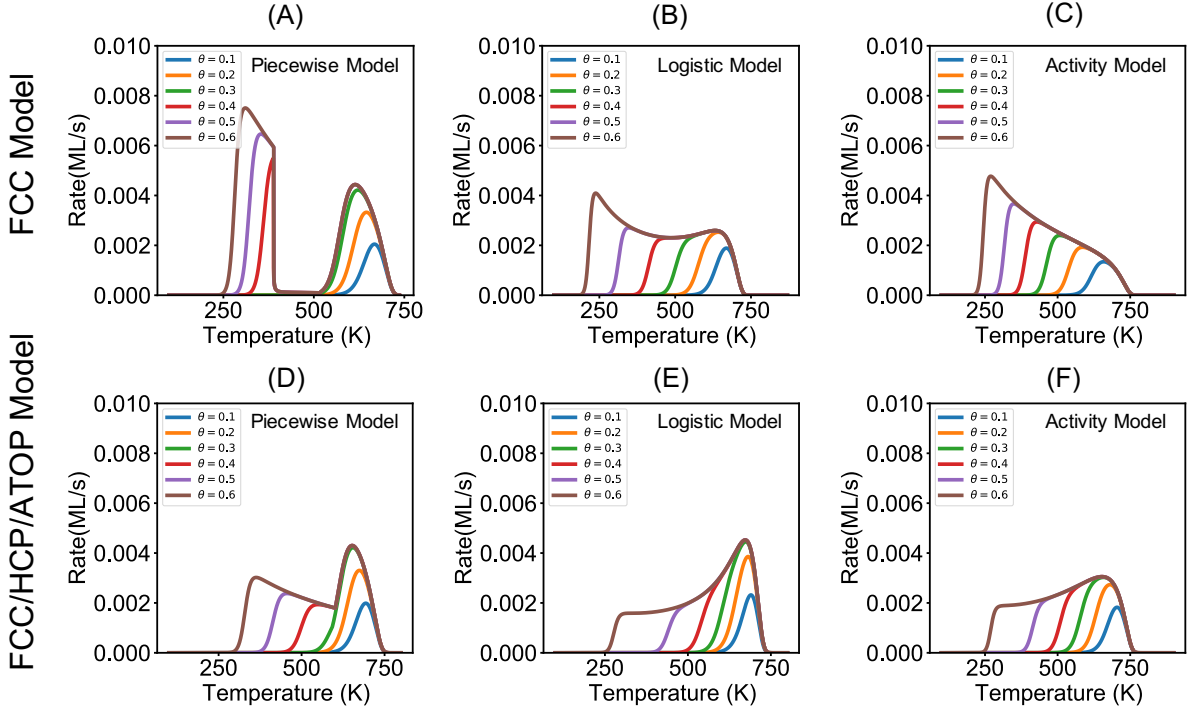


Figure 7: TPD Spectrum for the One and Three Site Model. (A) FCC Hollow Site Model, desorption rate is proportional to θ , (B) FCC, HCP Hollow, and Atop Site Model, desorption rate is proportional to θ

which is absent in the experimental TPD. In Figure 7 C, as initial coverage increase, the overall TPD trend are also increasing which is totally opposite to experimental TPD. Based on the TPD plot, it suggests that single site model cannot reflect actual coverage-dependent binding energy and TPD spectra varies also depend on the analytical model chosen.

Figure 7 D-F are TPD spectrum with different analytical fits of FCC/HCP/Atop model. As initial coverage up to 0.3 ML, Figure 7 D give a peak around 680K and peak shift slightly. When coverage increase to 0.4 ML, the TPD occur a polyline around 600K, and the reason is that piecewise function has an intersection point about 0.3 ML and the derivative is not continuous at that point so TPD has a turning point when initial coverage above 0.3 ML. Figure 7 E and F has the general shape that is more consistent with the experimental TPD. A low coverage peak occurs around 680 K, and grows until an initial coverage of 0.3 ML. The longer leading edge at higher coverages arises from the more gradual variation in the coverage-dependent binding energy. Although the shape of TPD spectra are different, the peak temperature stay constant within logistic and activity model. In section 4.3, fitting results show that piecewise function has the best fit result, but based on Figure 7 D-F, logistic function perform better in simulating TPD spectra.

358 **5 Conclusions**

359 A cluster expansion is a useful approach for exploring the coverage-dependent binding in multi-
360 site systems, such as CO on Pd(111). For CO adsorbed on Pd(111), inclusion of multiple sites in
361 CE is necessary to properly capture the coverage-dependent binding behavior. Using the cluster
362 expansion, GCMC simulations were used to extract the coverage-dependent binding energy ap-
363 propriately for mean-field models. Three analytical functions are used to fit coverage-dependent
364 binding energy for simulating TPD spectra. Three site model TPD can recover general shape
365 and high temperature peak compare to experimental result which indicate that combination of
366 cluster expansion and GCMC simulation can accurately capture coverage-dependent binding
367 energy of CO on Pd.

368

369 **Acknowledgment** This work was supported by the US Department of Energy Chemical
370 Sciences Program grant number DE-FG02-03ER15466. Computational support was provided
371 by the Notre Dame Center for Research Computing.

372 **References**

- 373 (1) Stampfl, C.; Kreuzer, H. J.; Payne, S. H.; Pfnür, H.; Scheffler, M. First-Principles Theory
374 of Surface Thermodynamics and Kinetics. *Physical Review Letters* **1999**, *83*, 2993–2996.
- 375 (2) Grabow, L. C.; Gokhale, A. A.; Evans, S. T.; Dumesic, J. A.; Mavrikakis, M. Mechanism
376 of the Water Gas Shift Reaction on Pt: First Principles, Experiments, and Microkinetic
377 Modeling. *The Journal of Physical Chemistry C* **2008**, *112*, 4608–4617.
- 378 (3) Gokhale, A. A.; Dumesic, J. A.; Mavrikakis, M. On the Mechanism of Low-Temperature
379 Water Gas Shift Reaction on Copper. *Journal of the American Chemical Society* **2008**,
380 *130*, 1402–1414.
- 381 (4) Getman, R. B.; Schneider, W. F. DFT-Based Coverage-Dependent Model of Pt-Catalyzed
382 NO Oxidation. *ChemCatChem* **2010**, *2*, 1450–1460.
- 383 (5) Grabow, L. C.; Hvolbæk, B.; Nørskov, J. K. Understanding Trends in Catalytic Activi-
384 ty: The Effect of Adsorbate-Adsorbate Interactions for CO Oxidation Over Transition
385 Metals. *Topics in Catalysis* **2010**, *53*, 298–310.
- 386 (6) Salciccioli, M.; Stamatakis, M.; Caratzoulas, S.; Vlachos, D. A Review of Multiscale
387 Modeling of Metal-Catalyzed Reactions: Mechanism Development for Complexity and
388 Emergent Behavior. *Chemical Engineering Science* **2011**, *66*, 4319–4355.
- 389 (7) Wu, C.; Schmidt, D.; Wolverton, C.; Schneider, W. Accurate Coverage-Dependence In-
390 corporated into First-Principles Kinetic Models: Catalytic NO Oxidation on Pt (111).
391 *Journal of Catalysis* **2012**, *286*, 88–94.
- 392 (8) Stamatakis, M. Kinetic Modelling of Heterogeneous Catalytic Systems. *Journal of Physics:*
393 *Condensed Matter* **2014**, *27*.
- 394 (9) Gomez-Marin, A. M.; Hernandez-Ortiz, J. P. Mean Field Approximation of Langmuir -
395 Hinshelwood CO - Surface Reactions Considering Lateral Interactions. *The Journal of
396 Physical Chemistry C* **2013**, *117*, 15716–15727.
- 397 (10) Guo, X.; Yates, J. T. Dependence of Effective Desorption Kinetic Parameters on Surface
398 Coverage and Adsorption Temperature: CO on Pd(111). *The Journal of Chemical Physics*
399 **1989**, *90*, 6761.

- 400 (11) Dulieu, F.; Congiu, E.; Noble, J.; Baouche, S.; Chaabouni, H.; Moudens, A.; Minissale, M.;
401 Cazaux, S. How Micron-Sized Dust Particles Determine the Chemistry of Our Universe.
402 *Scientific Reports* **2013**, *3*, 1338.
- 403 (12) Acharyya, K.; Fuchs, G. W.; Fraser, H. J.; van Dishoeck, E. F.; Linnartz, H. Desorption of
404 CO and O₂ Interstellar Ice Analogs. *Astronomy and Astrophysics* **2007**, *466*, 1005–1012.
- 405 (13) Shustorovich, E.; Sellers, H. The UBI-QEP Method: A Practical Theoretical Approach to
406 Understanding Chemistry on Transition Metal Surfaces. *Surface Science Reports* **1998**,
407 *31*, 1–119.
- 408 (14) Maestri, M.; Reuter, K. Semiempirical Rate Constants for Complex Chemical Kinetics:
409 First-Principles Assessment and Rational Refinement. *Angewandte Chemie* **2011**, *50*,
410 1194–1197.
- 411 (15) Miller, S. D.; Pushkarev, V. V.; Gellman, A. J.; Kitchin, J. R. Simulating Temperature
412 Programmed Desorption of Oxygen on Pt(111) Using DFT Derived Coverage Dependent
413 Desorption Barriers. *Topics in Catalysis* **2014**, *57*, 106–117.
- 414 (16) Tang, H.; Van Der Ven, A.; Trout, B. L. Lateral Interactions Between Oxygen Atoms
415 Adsorbed on Platinum (111) by First Principles. *Molecular Physics* **2004**, *102*, 273–279.
- 416 (17) Han, B.; Van der Ven, A.; Ceder, G.; Hwang, B.-J. Surface Segregation and Ordering of
417 Alloy Surfaces in the Presence of Adsorbates. *Physical Review B* **2005**, *72*, 205409.
- 418 (18) Miller, S. D.; Kitchin, J. R. Relating the Coverage Dependence of Oxygen Adsorption on
419 Au and Pt FCC(111) Surfaces Through Adsorbate-Induced Surface Electronic Structure
420 Effects. *Surface Science* **2009**, *603*, 794–801.
- 421 (19) Schmidt, D. J.; Chen, W.; Wolverton, C.; Schneider, W. F. Performance of Cluster Ex-
422 pansions of Coverage-Dependent Adsorption of Atomic Oxygen on Pt(111). *Journal of*
423 *Chemical Theory and Computation* **2012**, *8*, 264–273.
- 424 (20) Bray, J. M.; Smith, J. L.; Schneider, W. F. Coverage-Dependent Adsorption at a Low Sym-
425 metry Surface: DFT and Statistical Analysis of Oxygen Chemistry on Kinked Pt(321).
426 *Topics in Catalysis* **2014**, *57*, 89–105.
- 427 (21) Lerch, D.; Wieckhorst, O.; Hart, G. L. W.; Forcade, R. W.; Müller, S. UNCLE: A Code
428 for Constructing Cluster Expansions for Arbitrary Lattices with Minimal User-Input.
429 *Modelling and Simulation in Materials Science and Engineering* **2009**, *17*, 055003.

- 430 (22) Bray, J. M.; Schneider, W. F. In *Computational Catalysis*, Asthagiri, A., Janik, M., Eds.;
431 RSC Publishing: London, 2013.
- 432 (23) McEwen, J.-S.; Payne, S. H.; Stampfl, C. Phase Diagram of O/Ru (0001) from First
433 Principles. *Chemical Physics Letters* **2002**, *361*, 317–320.
- 434 (24) Lazo, C.; Keil, F. Phase Diagram of Oxygen Adsorbed on Ni(111) and Thermodynamic
435 Properties From First-Principles. *Physical Review B* **2009**, *79*, 245418.
- 436 (25) Chen, R.; Chen, Z.; Ma, B.; Hao, X.; Kapur, N.; Hyun, J.; Cho, K.; Shan, B. CO Adsorp-
437 tion on Pt(111) and Pd(111) Surfaces: A First-Principles Based Lattice Gas Monte-Carlo
438 Study. *Computational and Theoretical Chemistry* **2012**, *987*, 77–83.
- 439 (26) Tan, T. L.; Wang, L.-L.; Johnson, D. D.; Bai, K. Hydrogen Deposition on Pt(111) during
440 Electrochemical Hydrogen Evolution from a First-Principles Multiadsorption-Site Study.
441 *The Journal of Physical Chemistry C* **2013**, *117*, 22696–22704.
- 442 (27) Shan, B.; Zhao, Y.; Hyun, J.; Kapur, N.; Nicholas, J. B.; Cho, K. Coverage-Dependent CO
443 Adsorption Energy from First-Principles Calculations. *The Journal of Physical Chemistry*
444 *C* **2009**, *113*, 6088–6092.
- 445 (28) Lerch, D.; Wieckhorst, O.; Hammer, L.; Heinz, K.; Müller, S. Adsorbate Cluster Expan-
446 sion for an Arbitrary Number of Inequivalent Sites. *Physical Review B* **2008**, *78*, 121405.
- 447 (29) Sluiter, M.; Kawazoe, Y. Cluster Expansion Method for Adsorption: Application of Hy-
448 drogen Chemisorption on Graphene. *Physical Review B* **2003**, *68*, 085410.
- 449 (30) Stöhr, M.; Podloucky, R.; Müller, S. Ab initio Phase Diagram of Oxygen Adsorption on
450 W(110). *Journal of Physics: Condensed Matter* **2009**, *21*, 134017.
- 451 (31) Liu, D.-J.; Evans, J. W. Realistic Multisite Lattice-Gas Modeling and KMC Simulation of
452 Catalytic Surface Reactions: Kinetics and Multiscale Spatial Behavior for CO-Oxidation
453 on Metal (100) Surfaces. *Progress in Surface Science* **2013**, *88*, 393–521.
- 454 (32) Liu, D.-J.; Evans, J. W. Lattice-Gas Modeling of CO Adlayers on Pd(100). *The Journal*
455 *of Chemical Physics* **2004**, *121*, 4352–4357.
- 456 (33) Bollmann, L.; Ratts, J. L.; Joshi, A. M.; Williams, W. D.; Pazmino, J.; Joshi, Y. V.;
457 Miller, J. T.; Kropf, A. J.; Delgass, W. N.; Ribeiro, F. H. Effect of Zn Addition on the
458 Water–Gas Shift Reaction Over Supported Palladium Catalysts. *Journal of Catalysis*
459 **2008**, *257*, 43–54.

- 460 (34) Hilaire, S.; Wang, X.; Luo, T.; Gorte, R. J.; Wagner, J. A Comparative Study of Water-
461 Gas-Shift Reaction Over Ceria Supported Metallic Catalysts. *Applied Catalysis A: Gen-*
462 *eral* **2001**, *215*, 271–278.
- 463 (35) Kugai, J.; Fox, E. B.; Song, C. Role of CeO₂ Support for Pd-Cu Bimetallic Catalysts for
464 Oxygen-Enhanced Water Gas Shift. *Applied Catalysis A: General* **2013**, *456*, 204–214.
- 465 (36) Bunluesin, T.; Gottea, R. J.; Graham, G. W. Studies of the Water-Gas-Shift Reaction
466 on Ceria-Supported Pt, Pd, and Rh: Implications for Oxygen-Storage Properties. *Applied*
467 *Catalysis B: Environmental* **1998**, *15*, 107–114.
- 468 (37) Grenoble, D. C.; Estadt, M. M.; Ollis, D. F. The Chemistry and Catalysis of the Water
469 Gas Shift Reaction. *Journal of Catalysis* **1981**, *102*, 90–102.
- 470 (38) Olympiou, G. G.; Kalamaras, C. M.; Zeinalipour-Yazdi, C. D.; Efstatyiou, A. M. Mech-
471 anistic Aspects of the Water Gas Shift Reaction on Alumina-Supported Noble Metal
472 Catalysts: In situ DRIFTS and SSITKA-Mass Spectrometry Studies. *Catalysis Today*
473 **2007**, *127*, 304–318.
- 474 (39) Bariber Jr, J.; Duprez, D. Steam Effects in Three-Way Catalysis. *Applied Catalysis B:*
475 *Environmental* **1994**, *4*, 105–140.
- 476 (40) Phatak, A. A.; Koryabkina, N.; Rai, S.; Ratts, J. L.; Ruettinger, W.; Farrauto, R. J.;
477 Blau, G. E.; Delgass, W. N.; Ribeiro, F. H. Kinetics of the Water Gas Shift Reaction on
478 Pt Catalysts Supported on Alumina and Ceria. *Catalysis Today* **2007**, *123*, 224–234.
- 479 (41) Stamatakis, M.; Vlachos, D. G. A Graph-Theoretical Kinetic Monte Carlo Framework
480 for On-Lattice Chemical Kinetics. *The Journal of Chemical Physics* **2011**, *134*, 214115.
- 481 (42) Stamatakis, M.; Chen, Y.; Vlachos, D. G. First-Principles-Based Kinetic Monte Carlo
482 Simulation of the Structure Sensitivity of the Water Gas Shift Reaction on Platinum
483 Surfaces. *The Journal of Physical Chemistry C* **2011**, *115*, 24750–24762.
- 484 (43) Clay, J. P.; Greeley, J. P.; Ribeiro, F. H.; Delgass, W. N.; Schneider, W. F. DFT Com-
485 parison of Intrinsic WGS Kinetics over Pd and Pt. *Journal of Catalysis* **2014**, *320*, 106–
486 117.
- 487 (44) Tushaus, M.; Berndt, W.; Conrad, H.; Bradshaw, A. M.; Persson, B. Understanding the
488 Structure of High Coverage CO Adlayers. *Applied Physics A* **1990**, *51*, 91–98.

- 489 (45) Ohtani, H.; van Hove, M. A.; Somorjai, G. A. LEED Intensity Analysis of the Surface
490 Structures of Pd(111) in a $(\sqrt{3} \times \sqrt{3})$ -R30° Arrangement. *Surface Science* **1987**, *187*,
491 372–386.
- 492 (46) Rose, M. K.; Mitsui, T.; Dunphy, J.; Borg, A.; Ogletree, D. F.; Salmeron, M.; Sautet, P.
493 Ordered structures of CO on Pd(111) studied by STM. *Surface Science* **2002**, *512*, 48–60.
- 494 (47) Surnev, S.; Sock, M.; Ramsey, M. G.; Netzer, F. P.; Wiklund, M.; Borg, M.; Ander-
495 sen, J. N. CO adsorption on Pd(111): A High-Resolution Core Level Photoemission and
496 Electron Energy Loss Spectroscopy Study. *Surface Science* **2000**, *470*, 171–185.
- 497 (48) Bradshaw, A. M.; Hoffmann, F. M. The Chemisorption of Carbon Monoxide on Palla-
498 dium Single Crystal Surfaces: IR Spectroscopic Evidence for Loocalised Site Adsorption.
499 *Surface Science* **1978**, *72*, 513–535.
- 500 (49) Hoffmann, F. M. Infared Reflection-Absorption Spectroscopy of Adsorbed Molecules. *Sur-
501 face Science Reports* **1983**, *3*, 107–192.
- 502 (50) Gießel, T.; Schaff, O.; Hirschnugl, C. J.; Fernandez, V.; Schindler, K.-M.; Theobald, A.;
503 Bao, S.; Lindsay, R.; Berndt, W.; Bradshaw, A. M.; Baddeley, C.; Lee, A. F.; Lambert,
504 R. M.; Woodruff, D. P. A Photoelectron Diffraction Study of Ordered Structures in the
505 Chemisorption System Pd(111)-CO. *Surface Science* **1998**, *406*, 90–102.
- 506 (51) Conrad, H.; Ertl, G.; Koch, J.; Latta, E. E. Adsorption of CO on Pd Single Crystal
507 Surfaces. *Surface Science* **1974**, *43*, 462–480.
- 508 (52) Conrad, H.; Ertl, G.; Kuppers, J. Interactions Between Oxygen and Carbon Monoxide
509 on a Pd(111) Surface. *Surface Science* **1978**, *76*, 323–342.
- 510 (53) Sautet, P.; Rose, M. K.; Dunphy, J. C.; Behler, S.; Salmeron, M. Adsorption and Ener-
511 getics of Isolated CO Molecules on Pd(111). *Surface Science* **2000**, *453*, 25–31.
- 512 (54) Loffreda, D.; Simon, D.; Sautet, P. Dependence of Stretching Frequency on Surface Cov-
513 erage and Adsorbate–Adsorbate Interactions: A Density-Functional Theory Approach of
514 CO on Pd(111). *Surface Science* **1999**, *425*, 68–80.
- 515 (55) Herron, J. A.; Tonelli, S.; Mavrikakis, M. Atomic and Molecular Adsorption on Pd(111).
516 *Surface Science* **2012**, *606*, 1670–1679.

- 517 (56) Huang, S.-C.; Lin, C.-H.; Wang, J.-H. Trends of Water Gas Shift Reaction on Close-
518 Packed Transition Metal Surfaces. *The Journal of Physical Chemistry C* **2010**, *114*,
519 9826–9834.
- 520 (57) Lin, C.-H.; Chen, C.-l.; Wang, J.-H. Mechanistic Studies of Water Gas-Shift Reaction on
521 Transition Metals. *The Journal of Physical Chemistry B* **2011**, *115*, 18582–18588.
- 522 (58) Martin, N. M.; van den Bossche, M.; Gronbeck, H.; Hakanoglu, C.; Zhang, F.; Li, T.;
523 Gustafson, J.; Weaver, J. F.; Lundgren, E. CO Adsorption on Clean and Oxidized Pd
524 (111). *The Journal of Physical Chemistry C* **2014**, *118*, 1118–1128.
- 525 (59) Fernandez, V.; Gießel, T.; Schaff, O.; Schindler, K.-M.; Theobald, A.; Hirschlugl, C. J.;
526 Bao, S.; Bradshaw, A. M.; Baddeley, C.; Lee, A. F.; Lambert, R. M. A Photoelectron
527 Diffraction Study of the Pd(111) ($\sqrt{3} \times \sqrt{3}$)R30°–CO Chemisorption Phase. *Zeitschrift
528 für Physikalische Chemie* **1997**, *198*, 73–85.
- 529 (60) Kresse, G.; Furthmüller, J. Efficiency of ab initio Total Energy Calculations for Metals
530 and Semiconductors Using a Plane-Wave Basis Set. *Computational Materials Science*
531 **1996**, *6*, 15–50.
- 532 (61) Kresse, G.; Furthmüller, J. Efficient Iterative Schemes for ab initio Total-Energy Calcu-
533 lations Using a Plane-Wave Basis Set. *Physical Review B* **1996**, *54*, 11169–11186.
- 534 (62) Perdew, J. P.; Burke, K.; Ernzerhof, M. Generalized Gradient Approximation Made Sim-
535 ple. *Physical Review Letters* **1996**, *77*, 3865–3868.
- 536 (63) Perdew, J. P.; Wang, Y. Accurate and Simple Analytic Representation of the Electron-
537 Gas Correlation Energy. *Physical Review B* **1992**, *45*, 13244–13249.
- 538 (64) Kresse, G.; Joubert, D. From Ultrasoft Pseudopotentials to the Projector Augmented-
539 Wave Method. *Physical Review B* **1999**, *59*, 11–19.
- 540 (65) Bloch, P. E. Projector Augmented-Wave Method. *Physical Review B* **1994**, *50*, 17953–
541 17979.
- 542 (66) Davey, W. P. Precision Measurements of the Lattice Constants of Twelve Common Met-
543 als. *Physical Review* **1925**, *538*, 753–761.
- 544 (67) Monkhorst, H. J.; Pack, J. D. Special Points for Brillouin-Zone Integrations. *Physical
545 Review B* **1976**, *13*, 5188–5192.

- 546 (68) Nakamoto, K., *Infrared and Raman Spectra and Coordination Compounds*, Sixth; John
547 Wiley & Sons: Hoboken, New Jersey, 2009.
- 548 (69) Van de Walle, A. Multicomponent Multisublattice Alloys, Nonconfigurational Entropy
549 and Other Additions to the Alloy Theoretic Automated Toolkit. *CALPHAD: Computer*
550 *Coupling of Phase Diagrams and Thermochemistry* **2009**, *33*, 266–278.
- 551 (70) Van de Walle, A.; Asta, M. Self-Driven Lattice-Model Monte Carlo Simulations of Alloy
552 Thermodynamic Properties and Phase Diagrams. *Modeling and Simulations in Materials*
553 *Science and Engineering* **2002**, *10*, 521–538.
- 554 (71) Van de Walle, A.; Asta, M.; Ceder, G. The Alloy Theoretic Automated Toolkit: A User
555 Guide. *CALPHAD: Computer Coupling of Phase Diagrams and Thermochemistry* **2003**,
556 *26*, 539–553.
- 557 (72) Van de Walle, A.; Ceder, G. Automating First-Principle Phase Diagram Calculations.
558 *Journal of Phase Equilibria* **2002**, *23*, 348–359.
- 559 (73) Bray, J. M. Adsorbate Coverage Dependence in Heterogeneous Catalysis: Kinetics of
560 Oxygen on Platinum Surfaces From First Principles, Ph.D. Thesis, University of Notre
561 Dame, 2013.
- 562 (74) Zhang, P. Model Selection via Multifold Cross Validation. *The Annals of Statistics* **1993**,
563 *21*, 299–313.
- 564 (75) Shao, J. Linear Model Selection by Cross-Validation. *Journal of the American Statistical
565 Association* **1993**, *88*, 486–494.
- 566 (76) Arlot, S.; Celisse, A. A Survey of Cross-Validation Procedures for Model Selection. *Statistics
567 Surveys* **2010**, *4*, 40–79.
- 568 (77) Feibelman, P. J.; Hammer, B.; Nørskov, J. K.; Wagner, F.; Scheffler, M.; Stumpf, R.;
569 Watwe, R.; Dumesic, J. The CO/Pt(111) Puzzle. *The Journal of Physical Chemistry B*
570 **2001**, *105*, 4018–4025.
- 571 (78) Kresse, G.; Gil, A.; Sautet, P. Significance of Single-Electron Energies for the Description
572 of CO on Pt(111). *Physical Review B* **2003**, *68*, 073401.
- 573 (79) Park, Y. K.; Aghalayam, P.; Vlachos, D. G. A Generalized Approach for Predicting
574 Coverage-Dependent Reaction Parameters of Complex Surface Reactions: Application to
575 H₂ Oxidation over Platinum. *Journal of Physical Chemistry A* **1999**, *103*, 8101–8107.

- 576 (80) Aghalayam, P.; Park, Y. K.; Fernandes, N.; Papavassiliou, V.; Mhadeshwar, A. B.; Vla-
577 chos, D. G. A C1 Mechanism for Methane Oxidation on Platinum. *Journal of Catalysis*
578 **2003**, *213*, 23–38.
- 579 (81) Hansgen, D. A.; Vlachos, D. G.; Chen, J. G. Using First Principles to Predict Bimetallic
580 Catalysts for the Ammonia Decomposition Reaction. *Nature Chemistry* **2010**, *2*, 484–
581 489.
- 582 (82) Aghalayam, P.; Park, Y. K.; Vlachos, D. G. Construction and Optimization of Complex
583 Surface-Reaction Mechanisms. *AICHE Journal* **2000**, *46*, 2017–2029.
- 584 (83) Baker, B. G. Configurational Entropy of Adsorption of Large Atoms. *The Journal of
585 Chemical Physics* **1966**, *45*, 2694.
- 586 (84) Fowler, R. H. Adsorption Isotherms: Critical Isotherms. *Mathematical Proceedings of the
587 Cambridge Philosophical Society* **1936**, *32*, 144–151.
- 588 (85) Bajpai, A.; Frey, K.; Schneider, W. F. Comparison of Coverage-Dependent Binding En-
589 ergy Models for Mean-Field Microkinetic Rate Predictions. *Langmuir* **2020**, *36*, 465–
590 474.
- 591 (86) Redhead, P. A. Thermal Desorption of Gases. *Vacuum* **1962**, *12*, 203–211.
- 592 (87) Wellendorff, J.; Silbaugh, T. L.; Garcia-Pintos, D.; Nørskov, J. K.; Bligaard, T.; Studt,
593 F.; Campbell, C. T. A benchmark database for adsorption bond energies to transition
594 metal surfaces and comparison to selected DFT functionals. *Surface Science* **2015**, *640*,
595 36–44.

596 **Supplemental Information**

597 **S1 FCC Hollow Site Cluster Expansion**

598 The lat.in file sets up the CE and the adsorption sites. The file is used to create the structure
599 database and cluster database. The first line of the file sets up the unit cell. Lines 2-5 are the
600 unit cell vectors. The remaining lines set specify the atom positions and types.

601 The lat.in file for the FCC Hollow Site model is:

602 2.79658 2.79658 27.9658 90 90 60
603 1 0 0
604 0 1 0
605 0 0 1
606 0.0000000000000000 0.0000000000000000 0.0000000000000000 Pd_F
607 0.3333333333333333 0.3333333333333333 0.0817570000000032 Pd_F
608 0.6666666666666666 0.6666666666666666 0.1672046730538995 Pd_T
609 0.0000000000000000 0.0000000000000000 0.2168483413880288 Vac,CO_T

Table S1 Clusters Included in the Final FCC Hollow Site Cluster Expansion and Corresponding Interacting Coefficients. Cluster refers to the cluster number in the clusters.out file. Type refers to the number of sites in the cluster (1-body, 2-body, etc). ECIMULT is the ECI times the multiplicity and then converted from a per site basis to a per atom basis, and is used by ATAT.

Cluster	Type	Radius (Å)	Multiplicity	ECI ($\frac{eV}{site}$)	ECIMULT ($\frac{eV}{atom}$)
1	0	0.0000	1	-15.226	-3.80649
2	1	0.0000	1	-0.47508	-0.11877
3	2	2.79658	3	0.0816056	0.0612042

610 The clusters.out file contains all of the possible clusters that can be used in the fit. For each
611 cluster, each line has the following meaning:

612 Multiplicity

613 Radius

614 Number of Points in Cluster

615 [Coordinates of 1st point] [Number of possible species] [Cluster Function]

616 [Coordinates of 2nd point] [Number of possible species] [Cluster Function]

617 For the FCC Hollow Site model the clusters included are (each cluster separated by a blank
618 line):

619 1
620 0.00000
621 0
622
623 1
624 0.00000
625 1
626 1.00000 1.00000 0.21685 0 0
627
628 3
629 2.79658
630 2
631 1.00000 1.00000 0.21685 0 0
632 1.00000 -0.00000 0.21685 0 0

633 S2 FCC, and HCP Hollow Site Model

634 The lat.in file for the FCC, HCP Hollow Site model is:

```

635 2.79658 2.79658 27.9658 90 90 60
636 1 0 0
637 0 1 0
638 0 0 1
639 0.0000000000000000 0.0000000000000000 0.0000000000000000 Pd_F
640 0.3333333333333333 0.3333333333333333 0.0817570000000032 Pd_F
641 0.6666666666666666 0.6666666666666666 0.1672046730538995 Pd_T
642 0.0000000000000000 0.0000000000000000 0.2168483413880288 Vac,CO_T
643 0.3333333333333333 0.3333333333333333 0.2168483413880288 Vac,CO_T

```

Table S2 Clusters Included in the Final FCC, and HCP Hollow Site Cluster Expansion and Corresponding Interaction Coefficients. Cluster refers to the cluster number in the clusters.out file. Type refers to the number of sites in the cluster (1-body, 2-body, etc). ECIMULT is the ECI times the multiplicity and then converted from a per site basis to a per atom basis, and is used by ATAT.

Cluster	Type	Radius (Å)	Multiplicity	ECI ($\frac{\text{eV}}{\text{site}}$)	ECIMULT ($\frac{\text{eV}}{\text{atom}}$)
1	0	0.00000	1	0.59154	0.118318
2	1	0.00000	1	1.32978	0.265956
3	1	0.00000	1	1.65958	0.331916
4	2	1.61461	3	0.534113	0.320468
7	2	3.22921	3	0.14446	0.0866761
8	2	4.27185	6	0.018376	0.0220512
39	3	2.79658	1	-0.290463	-0.0580927
65	3	5.59316	1	-0.041425	-0.00828499
85	3	5.82155	3	0.010675	0.00640498
105	3	7.03791	6	-0.00239593	-0.00287512
162	3	8.07303	6	-0.00380084	-0.00456101
164	3	8.07303	3	0.00376478	0.00225887
180	3	8.38974	3	-0.018602	-0.0111612
181	3	8.38974	3	0.0147599	0.00885594

Table S2 *Continued*

Cluster	Type	Radius (Å)	Multiplicity	ECI ($\frac{\text{eV}}{\text{site}}$)	ECIMULT ($\frac{\text{eV}}{\text{atom}}$)
256	3	8.98975	6	-0.00497418	-0.00596901
279	3	9.68764	3	-0.00416738	-0.00250043
310	3	9.82127	6	0.00385753	0.00462904
329	4	3.22921	3	-0.0810983	-0.048659
330	4	3.22921	6	0.0814724	0.0977669
331	4	3.22921	3	-0.0894913	-0.0536948
332	4	4.27185	6	-0.0135723	-0.0162867
373	4	5.59316	6	0.0036217	0.00434604
378	4	5.59316	3	0.00858712	0.00515227
379	4	5.59316	3	-0.00923715	-0.00554229
417	4	5.82155	6	0.0206906	0.0248287
445	4	5.82155	6	-0.00237496	-0.00284995
466	4	5.82155	6	-0.0121338	-0.0145605
478	4	6.45842	6	0.00680341	0.00816409
505	4	6.45842	6	0.00674489	0.00809387
541	4	7.03791	6	-0.00924625	-0.0110955
549	4	7.03791	6	0.00826227	0.00991472
552	4	7.03791	3	-0.00867765	-0.00520659
574	4	7.03791	6	-0.00592294	-0.00710753
577	4	7.03791	6	0.00115571	0.00138685
620	4	7.39906	6	0.0117731	0.0141277
623	4	7.39906	6	0.00146167	0.001754
657	4	7.39906	6	-0.011727	-0.0140724
668	4	7.39906	6	0.00265795	0.00318954
681	4	7.39906	6	-0.00877475	-0.0105297
694	4	7.39906	6	0.0106109	0.0127331
717	4	7.39906	6	0.00233872	0.00280646
764	4	7.39906	6	0.00403757	0.00484509
795	4	7.39906	6	0.00318	0.003816

Table S2 *Continued*

Cluster	Type	Radius (Å)	Multiplicity	ECI ($\frac{\text{eV}}{\text{site}}$)	ECIMULT ($\frac{\text{eV}}{\text{atom}}$)
800	4	7.39906	6	-0.0132453	-0.0158943
807	4	7.39906	6	0.00436999	0.00524399
821	4	7.39906	6	-0.00744553	-0.00893464
839	4	7.39906	6	-0.00723076	-0.00867691

644 For the FCC, and HCP Hollow Site model the clusters included are (each cluster separated
 645 by a blank line):

646 1 667 3.22921
 647 0.00000 668 2
 648 0 669 0.33333 0.33333 0.21685 0 0
 649 670 1.00000 1.00000 0.21685 0 0
 650 1 671
 651 0.00000 672 6
 652 1 673 4.27185
 653 1.00000 1.00000 0.21685 0 0 674 2
 654 675 0.33333 0.33333 0.21685 0 0
 655 1 676 2.00000 0.00000 0.21685 0 0
 656 0.00000 677
 657 1 678 1
 658 0.33333 0.33333 0.21685 0 0 679 2.79658
 659 680 3
 660 3 681 0.33333 0.33333 0.21685 0 0
 661 1.61461 682 -0.66667 0.33333 0.21685 0 0
 662 2 683 -0.66667 1.33333 0.21685 0 0
 663 1.00000 1.00000 0.21685 0 0 684
 664 0.33333 1.33333 0.21685 0 0 685 1
 665 686 5.59316
 666 3 687 3

688	0.33333 0.33333 0.21685 0 0	719
689	0.33333 -1.66667 0.21685 0 0	720 3
690	2.33333 -1.66667 0.21685 0 0	721 8.38974
691		722 3
692	3	723 0.33333 0.33333 0.21685 0 0
693	5.82155	724 1.00000 -2.00000 0.21685 0 0
694	3	725 3.33333 -2.66667 0.21685 0 0
695	0.33333 0.33333 0.21685 0 0	726
696	-0.66667 0.33333 0.21685 0 0	727 3
697	1.00000 -2.00000 0.21685 0 0	728 8.38974
698		729 3
699	6	730 0.33333 0.33333 0.21685 0 0
700	7.03791	731 3.00000 0.00000 0.21685 0 0
701	3	732 3.33333 -2.66667 0.21685 0 0
702	0.33333 0.33333 0.21685 0 0	733
703	0.33333 -0.66667 0.21685 0 0	734 6
704	3.00000 -2.00000 0.21685 0 0	735 8.98975
705		736 3
706	6	737 1.00000 1.00000 0.21685 0 0
707	8.07303	738 4.00000 0.00000 0.21685 0 0
708	3	739 3.33333 -2.66667 0.21685 0 0
709	1.00000 1.00000 0.21685 0 0	740
710	0.33333 1.33333 0.21685 0 0	741 3
711	-0.66667 4.33333 0.21685 0 0	742 9.68764
712		743 3
713	3	744 0.33333 0.33333 0.21685 0 0
714	8.07303	745 0.00000 0.00000 0.21685 0 0
715	3	746 -1.66667 -1.66667 0.21685 0 0
716	1.00000 1.00000 0.21685 0 0	747
717	0.33333 2.33333 0.21685 0 0	748 6
718	-0.66667 4.33333 0.21685 0 0	749 9.82127
		750 3

```

751 1.00000 1.00000 0.21685 0 0
752 0.00000 1.00000 0.21685 0 0
753 -2.66667 4.33333 0.21685 0 0
754
755 3
756 3.22921
757 4
758 0.33333 0.33333 0.21685 0 0
759 1.00000 0.00000 0.21685 0 0
760 0.33333 1.33333 0.21685 0 0
761 1.00000 1.00000 0.21685 0 0
762
763 6
764 3.22921
765 4
766 0.33333 0.33333 0.21685 0 0
767 0.00000 1.00000 0.21685 0 0
768 0.33333 1.33333 0.21685 0 0
769 1.00000 1.00000 0.21685 0 0
770
771 3
772 3.22921
773 4
774 1.00000 1.00000 0.21685 0 0
775 1.33333 0.33333 0.21685 0 0
776 0.33333 1.33333 0.21685 0 0
777 0.33333 0.33333 0.21685 0 0
778
779 6
780 4.27185
781 4
782 0.33333 0.33333 0.21685 0 0
783 1.00000 0.00000 0.21685 0 0
784 0.33333 1.33333 0.21685 0 0
785 2.00000 0.00000 0.21685 0 0
786
787 6
788 5.59316
789 4
790 0.33333 0.33333 0.21685 0 0
791 1.00000 0.00000 0.21685 0 0
792 2.00000 0.00000 0.21685 0 0
793 2.33333 -1.66667 0.21685 0 0
794
795 3
796 5.59316
797 4
798 0.33333 0.33333 0.21685 0 0
799 0.33333 -0.66667 0.21685 0 0
800 1.33333 -1.66667 0.21685 0 0
801 2.33333 -1.66667 0.21685 0 0
802
803 3
804 5.59316
805 4
806 0.33333 0.33333 0.21685 0 0
807 1.33333 0.33333 0.21685 0 0
808 1.33333 -1.66667 0.21685 0 0
809 2.33333 -1.66667 0.21685 0 0
810
811 6
812 5.82155
813 4

```

814	1.00000	1.00000	0.21685	0	0	845	4				
815	0.33333	1.33333	0.21685	0	0	846	1.00000	1.00000	0.21685	0	0
816	0.33333	2.33333	0.21685	0	0	847	0.00000	2.00000	0.21685	0	0
817	-0.66667	3.33333	0.21685	0	0	848	-0.66667	3.33333	0.21685	0	0
818						849	-1.66667	2.33333	0.21685	0	0
819	6					850					
820	5.82155					851	6				
821	4					852	7.03791				
822	0.33333	0.33333	0.21685	0	0	853	4				
823	1.00000	0.00000	0.21685	0	0	854	1.00000	1.00000	0.21685	0	0
824	0.33333	-0.66667	0.21685	0	0	855	0.00000	1.00000	0.21685	0	0
825	1.00000	-2.00000	0.21685	0	0	856	-0.66667	3.33333	0.21685	0	0
826						857	-1.66667	3.33333	0.21685	0	0
827	6					858					
828	5.82155					859	6				
829	4					860	7.03791				
830	0.33333	0.33333	0.21685	0	0	861	4				
831	0.33333	-0.66667	0.21685	0	0	862	1.00000	1.00000	0.21685	0	0
832	-0.66667	-0.66667	0.21685	0	0	863	0.00000	1.00000	0.21685	0	0
833	1.00000	-2.00000	0.21685	0	0	864	-1.66667	2.33333	0.21685	0	0
834						865	-1.66667	3.33333	0.21685	0	0
835	6					866					
836	6.45842					867	3				
837	4					868	7.03791				
838	0.33333	0.33333	0.21685	0	0	869	4				
839	1.33333	-0.66667	0.21685	0	0	870	1.00000	1.00000	0.21685	0	0
840	2.00000	0.00000	0.21685	0	0	871	0.33333	1.33333	0.21685	0	0
841	3.00000	-1.00000	0.21685	0	0	872	-1.66667	1.33333	0.21685	0	0
842						873	-1.66667	3.33333	0.21685	0	0
843	6					874					
844	6.45842					875	6				
						876	7.03791				

		908	7.39906
877	4	909	4
878	0.33333 0.33333 0.21685 0 0	910	0.33333 0.33333 0.21685 0 0
879	1.33333 0.33333 0.21685 0 0	911	0.00000 1.00000 0.21685 0 0
880	2.33333 -0.66667 0.21685 0 0	912	-2.66667 2.33333 0.21685 0 0
881	3.00000 -2.00000 0.21685 0 0	913	-1.66667 3.33333 0.21685 0 0
882		914	
883	6	915	6
884	7.03791	916	7.39906
885	4	917	4
886	0.33333 0.33333 0.21685 0 0	918	0.33333 0.33333 0.21685 0 0
887	1.33333 0.33333 0.21685 0 0	919	1.00000 1.00000 0.21685 0 0
888	2.33333 0.33333 0.21685 0 0	920	1.33333 2.33333 0.21685 0 0
889	3.00000 -2.00000 0.21685 0 0	921	-1.66667 3.33333 0.21685 0 0
890		922	
891	6	923	6
892	7.39906	924	7.39906
893	4	925	4
894	0.33333 0.33333 0.21685 0 0	926	1.00000 1.00000 0.21685 0 0
895	-1.00000 1.00000 0.21685 0 0	927	1.33333 1.33333 0.21685 0 0
896	1.33333 1.33333 0.21685 0 0	928	2.33333 0.33333 0.21685 0 0
897	-1.66667 3.33333 0.21685 0 0	929	4.00000 0.00000 0.21685 0 0
898		930	
899	6	931	6
900	7.39906	932	7.39906
901	4	933	4
902	0.33333 0.33333 0.21685 0 0	934	1.00000 1.00000 0.21685 0 0
903	0.33333 1.33333 0.21685 0 0	935	1.33333 1.33333 0.21685 0 0
904	-0.66667 2.33333 0.21685 0 0	936	2.33333 1.33333 0.21685 0 0
905	-1.66667 3.33333 0.21685 0 0	937	4.00000 0.00000 0.21685 0 0
906		938	
907	6	939	6

940	7.39906	967	1.00000 0.00000 0.21685 0 0
941	4	968	2.33333 -1.66667 0.21685 0 0
942	1.00000 1.00000 0.21685 0 0	969	2.33333 -2.66667 0.21685 0 0
943	2.00000 1.00000 0.21685 0 0	970	
944	3.00000 1.00000 0.21685 0 0	971	6
945	4.00000 0.00000 0.21685 0 0	972	7.39906
946		973	4
947	6	974	0.33333 0.33333 0.21685 0 0
948	7.39906	975	1.00000 0.00000 0.21685 0 0
949	4	976	1.00000 -2.00000 0.21685 0 0
950	0.33333 0.33333 0.21685 0 0	977	2.33333 -2.66667 0.21685 0 0
951	1.00000 0.00000 0.21685 0 0	978	
952	0.33333 -0.66667 0.21685 0 0	979	6
953	2.33333 -2.66667 0.21685 0 0	980	7.39906
954		981	4
955	6	982	0.33333 0.33333 0.21685 0 0
956	7.39906	983	1.33333 -0.66667 0.21685 0 0
957	4	984	0.00000 -2.00000 0.21685 0 0
958	0.33333 0.33333 0.21685 0 0	985	2.33333 -2.66667 0.21685 0 0
959	0.00000 0.00000 0.21685 0 0	986	
960	2.33333 -0.66667 0.21685 0 0	987	6
961	2.33333 -2.66667 0.21685 0 0	988	7.39906
962		989	4
963	6	990	1.00000 1.00000 0.21685 0 0
964	7.39906	991	2.33333 0.33333 0.21685 0 0
965	4	992	1.33333 -0.66667 0.21685 0 0
966	0.33333 0.33333 0.21685 0 0	993	3.00000 -2.00000 0.21685 0 0

994 **S3 FCC, HCP Hollow, and Atop Site Model**

995 The lat.in file for the FCC, HCP Hollow and Atop Site model is:

```

996 2.79658 2.79658 27.9658 90 90 60
997 1 0 0
998 0 1 0
999 0 0 1
1000 0.0000000000000000 0.0000000000000000 0.0000000000000000 Pd_F
1001 0.3333333333333333 0.3333333333333333 0.0817570000000032 Pd_F
1002 0.6666666666666666 0.6666666666666666 0.1672046730538995 Pd_T
1003 0.0000000000000000 0.0000000000000000 0.2168483413880288 Vac,CO_T
1004 0.3333333333333333 0.3333333333333333 0.2168483413880288 Vac,CO_T
1005 0.6666666666666666 0.6666666666666666 0.2190000000000000 Vac,CO_T

```

Table S3 Clusters Included in the Final FCC, HCP Hollow, and Atop Site Cluster Expansion and Corresponding Interaction Coefficients. Cluster refers to the cluster number in the clusters.out file. Type refers to the number of sites in the cluster (1-body, 2-body, etc). ECIMULT is the ECI times the multiplicity and then converted from a per site basis to a per atom basis, and is used by ATAT.

Cluster	Type	Radius (Å)	Multiplicity	ECI ($\frac{\text{eV}}{\text{site}}$)	ECIMULT ($\frac{\text{eV}}{\text{atom}}$)
1	0	0.0000	1	15.95998	2.65999
2	1	0.0000	1	1.08805	0.18134
3	1	0.0000	1	1.26703	0.21117
4	1	0.0000	1	1.20919	0.20153
5	2	1.61461	3	-0.148341	-0.0741707
8	2	2.79658	3	0.0536316	0.0268158
11	2	3.22921	3	0.072558	0.036279
14	2	4.27185	6	0.022161	0.022161
19	2	4.84382	3	0.0743748	0.0371874
21	2	5.59316	3	-0.0248188	-0.0124094
71	3	1.61573	6	-0.244403	-0.244403
76	3	2.79658	3	-0.126501	-0.0632507
80	3	2.79658	3	-0.0762564	-0.0381282

Table S3 *Continued*

Cluster	Type	Radius (Å)	Multiplicity	ECI ($\frac{\text{eV}}{\text{site}}$)	ECIMULT ($\frac{\text{eV}}{\text{atom}}$)
84	3	3.22921	6	-0.000740649	-0.000740649
91	3	3.22977	6	-0.00504543	-0.00504543
94	3	4.27185	6	0.0218627	0.0218627
125	3	4.84382	6	-0.00253411	-0.00253411
133	3	4.84382	6	0.00823612	0.00823612
144	3	4.84382	3	0.0570202	0.0285101
183	3	5.82155	3	-0.00564352	-0.00282176
217	3	5.82186	3	0.050182	0.025091
251	3	6.45842	6	-0.00558862	-0.00558862
263	3	6.45871	3	-0.020762	-0.010381
274	3	6.45871	6	0.0046538	0.0046538
307	3	7.03816	6	-0.0284037	-0.0284037
391	3	7.39906	6	-0.00401469	-0.00401469
395	3	7.39906	3	0.00218226	0.00109113
450	3	7.39906	6	0.0060388	0.0060388
479	3	8.07326	6	-0.00333807	-0.00333807
555	3	8.38974	6	0.00197207	0.00197207
649	3	8.5439	6	0.00397997	0.00397997
656	3	8.5439	6	0.00391244	0.00391244
673	3	8.5439	3	-0.00572324	-0.00286162
706	3	8.98975	6	0.00668111	0.00668111
807	3	8.98995	6	-0.0111084	-0.0111084
826	3	8.98995	6	-0.00774344	-0.00774344
840	3	9.68764	6	0.0141938	0.0141938
874	3	9.68764	6	-0.00152421	-0.00152421
889	3	9.68764	6	-0.0142386	-0.0142386
903	3	9.68764	3	0.0109553	0.00547766
923	3	9.82127	6	-0.00492306	-0.00492306
946	3	9.82127	6	0.00431624	0.00431624

Table S3 *Continued*

Cluster	Type	Radius (Å)	Multiplicity	ECI ($\frac{\text{eV}}{\text{site}}$)	ECIMULT ($\frac{\text{eV}}{\text{atom}}$)
975	3	9.82145	6	-0.0109474	-0.0109474

1006 For the FCC, HCP Hollow, and Atop Site model the clusters included are (each cluster
 1007 separated by a blank line):

1008 1		1032			
1009 0.00000		1033	3		
1010 0		1034	2.79658		
1011		1035	2		
1012 1		1036	0.666667 0.666667 0.21900 0 0		
1013 0.00000		1037	1.666667 -0.333333 0.21900 0 0		
1014 1		1038			
1015 1.00000 1.00000 0.21685 0 0		1039	3		
1016		1040	3.22921		
1017 1		1041	2		
1018 0.00000		1042	0.333333 0.333333 0.21685 0 0		
1019 1		1043	1.000000 1.000000 0.21685 0 0		
1020 0.333333 0.333333 0.21685 0 0		1044			
1021		1045	6		
1022 1		1046	4.27185		
1023 0.00000		1047	2		
1024 1		1048	0.333333 0.333333 0.21685 0 0		
1025 0.666667 0.666667 0.21900 0 0		1049	2.000000 0.000000 0.21685 0 0		
1026		1050			
1027 3		1051	3		
1028 1.61461		1052	4.84382		
1029 2		1053	2		
1030 1.00000 1.00000 0.21685 0 0		1054	0.333333 0.333333 0.21685 0 0		
1031 0.333333 1.333333 0.21685 0 0		1055	1.333333 -1.666667 0.21685 0 0		

1056		1087	0.33333 0.33333 0.21685 0 0
1057	3	1088	1.00000 0.00000 0.21685 0 0
1058	5.59316	1089	1.00000 1.00000 0.21685 0 0
1059	2	1090	
1060	0.66667 0.66667 0.21900 0 0	1091	6
1061	2.66667 0.66667 0.21900 0 0	1092	3.22977
1062		1093	3
1063	6	1094	0.66667 0.66667 0.21900 0 0
1064	1.61573	1095	0.33333 1.33333 0.21685 0 0
1065	3	1096	-0.66667 1.33333 0.21685 0 0
1066	1.00000 1.00000 0.21685 0 0	1097	
1067	0.33333 1.33333 0.21685 0 0	1098	6
1068	0.66667 0.66667 0.21900 0 0	1099	4.27185
1069		1100	3
1070	3	1101	0.33333 0.33333 0.21685 0 0
1071	2.79658	1102	1.00000 0.00000 0.21685 0 0
1072	3	1103	2.00000 0.00000 0.21685 0 0
1073	1.00000 1.00000 0.21685 0 0	1104	
1074	1.33333 0.33333 0.21685 0 0	1105	6
1075	2.00000 0.00000 0.21685 0 0	1106	4.84382
1076		1107	3
1077	3	1108	1.00000 1.00000 0.21685 0 0
1078	2.79658	1109	0.00000 2.00000 0.21685 0 0
1079	3	1110	0.00000 3.00000 0.21685 0 0
1080	0.33333 0.33333 0.21685 0 0	1111	
1081	0.00000 1.00000 0.21685 0 0	1112	6
1082	-0.66667 1.33333 0.21685 0 0	1113	4.84382
1083		1114	3
1084	6	1115	0.33333 0.33333 0.21685 0 0
1085	3.22921	1116	1.00000 0.00000 0.21685 0 0
1086	3	1117	1.33333 -1.66667 0.21685 0 0
		1118	

			1150	0.666667	0.666667	0.21900	0	0
1119	3		1151	0.00000	2.00000	0.21685	0	0
1120	4.84382		1152	-0.666667	3.33333	0.21685	0	0
1121	3		1153					
1122	0.33333	0.33333	0.21685	0	0	1154	6	
1123	0.00000	0.00000	0.21685	0	0	1155	6.45871	
1124	-0.666667	-0.666667	0.21685	0	0	1156	3	
1125			1157	0.33333	0.33333	0.21685	0	0
1126	3		1158	-0.33333	-0.33333	0.21900	0	0
1127	5.82155		1159	-2.33333	1.666667	0.21900	0	0
1128	3		1160					
1129	1.00000	1.00000	0.21685	0	0	1161	6	
1130	0.00000	1.00000	0.21685	0	0	1162	7.03816	
1131	-0.666667	3.33333	0.21685	0	0	1163	3	
1132			1164	0.666667	0.666667	0.21900	0	0
1133	3		1165	1.666667	0.666667	0.21900	0	0
1134	5.82186		1166	0.33333	3.33333	0.21685	0	0
1135	3		1167					
1136	0.666667	0.666667	0.21900	0	0	1168	6	
1137	1.666667	0.666667	0.21900	0	0	1169	7.39906	
1138	2.33333	-1.666667	0.21685	0	0	1170	3	
1139			1171	1.00000	1.00000	0.21685	0	0
1140	6		1172	1.33333	0.33333	0.21685	0	0
1141	6.45842		1173	4.00000	0.00000	0.21685	0	0
1142	3		1174					
1143	1.00000	1.00000	0.21685	0	0	1175	3	
1144	0.00000	3.00000	0.21685	0	0	1176	7.39906	
1145	-1.666667	2.33333	0.21685	0	0	1177	3	
1146			1178	1.00000	1.00000	0.21685	0	0
1147	3		1179	1.00000	2.00000	0.21685	0	0
1148	6.45871		1180	4.00000	0.00000	0.21685	0	0
1149	3		1181					

1182	6	1213	0.666667	0.666667	0.21900	0	0
1183	7.39906	1214	2.333333	1.333333	0.21685	0	0
1184	3	1215	4.000000	-2.000000	0.21685	0	0
1185	1.000000	1.000000	0.21685	0	0	1216	
1186	0.333333	-0.666667	0.21685	0	0	1217	3
1187	3.000000	-2.000000	0.21685	0	0	1218	8.5439
1188		1219	3				
1189	6	1220	1.000000	1.000000	0.21685	0	0
1190	8.07326	1221	3.000000	1.000000	0.21685	0	0
1191	3	1222	3.666667	-2.333333	0.21900	0	0
1192	1.000000	1.000000	0.21685	0	0	1223	
1193	0.333333	3.333333	0.21685	0	0	1224	6
1194	2.666667	2.666667	0.21900	0	0	1225	8.98975
1195		1226	3				
1196	6	1227	0.333333	0.333333	0.21685	0	0
1197	8.38974	1228	1.666667	-0.333333	0.21900	0	0
1198	3	1229	4.000000	-2.000000	0.21685	0	0
1199	1.000000	1.000000	0.21685	0	0	1230	
1200	2.000000	0.000000	0.21685	0	0	1231	6
1201	1.000000	-2.000000	0.21685	0	0	1232	8.98995
1202		1233	3				
1203	6	1234	0.666667	0.666667	0.21900	0	0
1204	8.5439	1235	2.666667	-1.333333	0.21900	0	0
1205	3	1236	2.000000	-3.000000	0.21685	0	0
1206	0.666667	0.666667	0.21900	0	0	1237	
1207	2.000000	-1.000000	0.21685	0	0	1238	6
1208	4.000000	-2.000000	0.21685	0	0	1239	8.98995
1209		1240	3				
1210	6	1241	1.000000	1.000000	0.21685	0	0
1211	8.5439	1242	-0.333333	2.666667	0.21900	0	0
1212	3	1243	-0.333333	4.666667	0.21900	0	0
		1244					

1245	6		1269	1.00000	1.00000	0.21685	0	0			
1246	9.68764		1270	0.66667	0.66667	0.21900	0	0			
1247	3		1271	-1.00000	-1.00000	0.21685	0	0			
1248	0.66667	0.66667	0.21900	0	0	1272					
1249	1.00000	-1.00000	0.21685	0	0	1273	6				
1250	2.66667	-3.33333	0.21900	0	0	1274	9.82127				
1251			1275	3		1276	0.33333	0.33333	0.21685	0	0
1252	6		1277	0.00000	-1.00000	0.21685	0	0			
1253	9.68764		1278	4.00000	-3.00000	0.21685	0	0			
1254	3		1279			1280	6				
1255	1.00000	1.00000	0.21685	0	0	1281	9.82127				
1256	1.00000	-1.00000	0.21685	0	0	1282	3				
1257	3.00000	-3.00000	0.21685	0	0	1283	1.00000	1.00000	0.21685	0	0
1258			1284	0.33333	2.33333	0.21685	0	0			
1259	6		1285	-2.66667	4.33333	0.21685	0	0			
1260	9.68764		1286			1287	6				
1261	3		1288	9.82145		1289	3				
1262	0.66667	0.66667	0.21900	0	0	1290	0.33333	0.33333	0.21685	0	0
1263	2.00000	-2.00000	0.21685	0	0	1291	2.00000	0.00000	0.21685	0	0
1264	-1.33333	-1.33333	0.21900	0	0	1292	3.66667	-3.33333	0.21900	0	0
1265			1293			1294					
1266	3		1295			1296					
1267	9.68764		1297			1298					
1268	3		1299			1300					

1293 S4 Entropy Treatment

1294 The differential configurational entropy is derived based on the strategy developed from Baker
 1295 [83]. Considering the surface has N atoms and total available site is n^*N , n is number of site
 1296 per atom. Now assume the surface has x adsorbate and $x < N$.

$$S = k_B * \ln W \quad (\text{S1})$$

1297 Here W is the number of configuration of adsorbates on surface.

$$W = \frac{n * N * [n * N - b_1] * [n * N - (b_1 + b_2)] \cdots [n * N - (\sum_{i=1}^{x-1} b_i)]}{x!} \quad (\text{S2})$$

$$\begin{aligned} S &= k_B * \ln W \\ &= k_B * [\ln(n * N) + \ln(n * N - b_1) + \ln(n * N - (b_1 + b_2)) + \cdots + \ln(n * N - (\sum_{i=1}^{x-1} b_i)) - \ln(x!)] \end{aligned} \quad (\text{S3})$$

1298 Differential configurational entropy \bar{S} can be derived by:

$$\begin{aligned} \bar{S} &= \frac{\partial S}{\partial x} \\ &= k_B * [\ln(n * N - (\sum_{i=1}^{x-1} b_i)) - \ln(x + 1)] \end{aligned} \quad (\text{S4})$$

1299 Since $x \gg 1$, so $x + 1 \approx x$ and $\sum_{i=1}^{x-1} b_i = x * \bar{\nu}$, $\bar{\nu}$ is occupation number defined by number of
 1300 site blocked divided by number of adsorbate,

$$\begin{aligned} \bar{S} &= k_B * [\ln(n * N - x * \bar{\nu}) - \ln(x)] \\ &= -k_B * [\ln(\frac{x}{n * N - x * \bar{\nu}})] \end{aligned} \quad (\text{S5})$$

1301 Here we define $\theta = \frac{x}{N}$, and we consider adsorbates interaction, so if one CO occupied FCC site,
 1302 adjacent HCP site cannot be occupied by another CO, therefore, $n = \bar{\nu}$ in this scenario. Based
 1303 on this assumption, we can simplify the equation S5 to

$$\bar{S} = -k_B * [\ln(\frac{\theta}{n * (1 - \theta)})] \quad (\text{S6})$$

1304 S5 Model Comparison

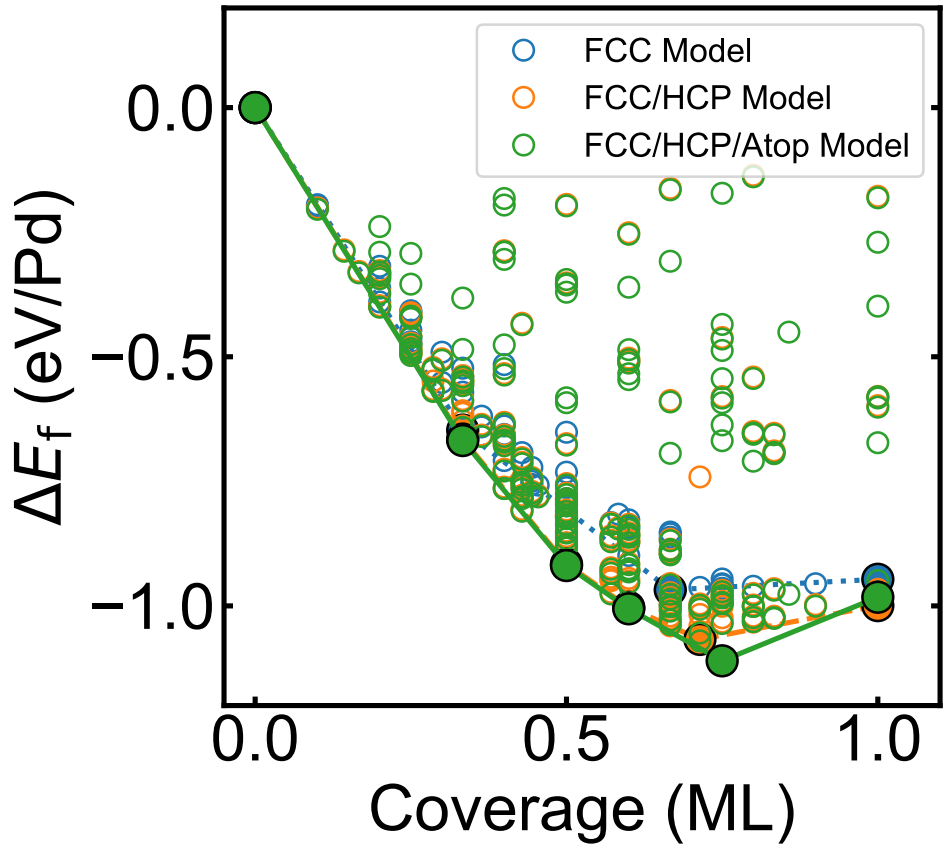


Figure S1: Comparison of DFT Formation Energies (ΔE_f) Between the Three Cluster Expansion Models

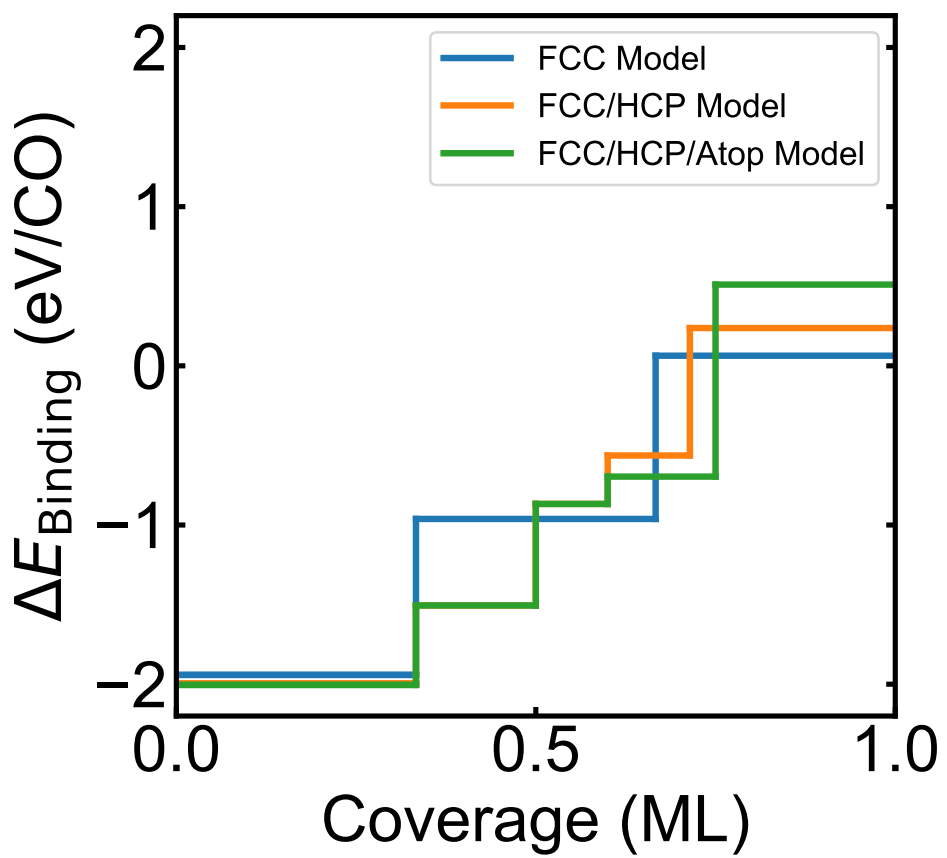


Figure S2: Comparison of Differential Binding Energy ($\Delta E_{\text{Binding}}(\theta)$) Between the Three Cluster Expansion Models